JOURNAL OF GEOPHYSICAL RESEARCH, VOL. 104, NO. D22, PAGES 27,253–27,275, NOVEMBER 27, 1999

# Decadal climate variability in a coupled atmosphere-ocean climate model of moderate complexity

Dörthe Handorf,[1] Vladimir K. Petoukhov,[2] Klaus Dethloff,[1]
Alexey V. Eliseev,[2] Antje Weisheimer,[1] and Igor I. Mokhov[2]

**Abstract.** In this study we determined characteristic temporal modes of atmospheric variability at the decadal and interdecadal timescales. This was done on the basis of 1000 year long integrations of a global coupled atmosphere-ocean climate model of moderate complexity including the troposphere, stratosphere, and mesosphere. The applied model resolves explicitely the basic features of the large-scale long-term atmospheric and oceanic variables. The synoptic-scale processes are described in terms of autocorrelation and crosscorrelation functions. The paper includes an extended description and validation of the model as well as the results of analyses of two 1000 year long model integrations. One model run has been performed with the fully coupled model of the atmosphere-ocean system. The performed time-frequency analyses of atmospheric fields reveal strong decadal and interdecadal modes with periods of about 9, 18, and 30 years. To quantify the influence of the ocean on atmospheric variations an additional run with seasonally varying prescribed sea surface temperatures has been carried out, which is characterized by strong decadal modes with periods of about 9 years. The comparison of both runs suggests that decadal variability can be understood as an inherent atmospheric mode due to the nonlinear dynamics of the large-scale atmospheric circulation patterns whereas interdecadal climate variability has to be regarded as coupled atmosphere-ocean modes.

## 1. Introduction

As possible causes of climate variations on timescales of decades to centuries, nonlinear atmospheric variability, nonlinear interactions in the atmosphere-ocean system, and variability of external factors, such as solar radiation, aerosol loading, and atmospheric trace gas concentrations, have been discussed. While external factors including anthropogenic effects have been extensively investigated, the knowledge of the contribution of nonlinear atmospheric processes to climate processes is rather poor. The atmosphere fluctuates on a broad timescale and undergoes strong interannual variations, but the mechanisms of this variability are not yet understood. This shortcoming exists in particular as a result of the absence of statistically sufficient long atmospheric observational data series and as a result of the limits of temporal and horizontal resolution of paleoclimate proxy data analysis. To address the problem of internal low-frequency variability anyway, long-term integrations of appropriate models are one possible way to get hints on the real atmospheric behavior on the decadal and interdecadal timescales.

The study of the internal low-frequency variability generation in simple low-order and complex atmospheric and coupled atmosphere-ocean circulation models started with the work by *James and James* [1989]. They used a primitive equation model of the atmosphere to produce pronounced internal climate variability on the interannual and decadal timescales. The decadal climate variability was associated with fluctuations of the unstable baroclinic waves in midlatitudes [*James and James,* 1992]. In the work of *James et al.* [1994] it was shown that the atmospheric low-frequency variability was caused not only by stochastic contributions but also by the low-dimensional nonlinear dynamics. The influence of nonlinear dynamics on the long-term climate variability in simple atmospheric low-order models was investigated by *Pielke and Zeng* [1994] and *Kurgansky et al.* [1996].

The role of orographic, thermal, and synoptic influences in producing the long-term climate variability was investigated by *Dethloff et al.* [1998] using an atmosphere-like, dynamical low-order system which has

[1]Alfred Wegener Institute for Polar and Marine Research, Potsdam, Germany.
[2]Obukhov Institute of Atmospheric Physics, Moscow.



Paper number 1999JD900836.
0148-0227/99/1999JD900836$09.00

been integrated over 10,000 years. The system reproduces a natural variability on decadal and centenary timescales. The natural variability is understood as fluctuations of the climatic system due to internal interactions associated with nonlinear mechanisms and instability processes.

*Saravanan and McWilliams* [1997] used an idealized atmosphere-ocean model with an intermediate degree of complexity consisting of a T21 two-level atmospheric model coupled to a zonally averaged sector ocean model to investigate climatic variability on interdecadal timescales. Atmospheric variability on interannual and longer timescales in this idealized model is dominated by a small number of preferred spatial patterns similar to teleconnection patterns but without preferred time periods.

Integrations with complex coupled general circulation models (GCM) of the atmosphere-ocean system over 500-1000 years have been described, for example, by *Manabe and Stouffer* [1996], *Hunt and Davies* [1997], *Tett et al.* [1997], and *von Storch et al.* [1997], whereby in all these complex GCMs a seasonally varying flux correction term had to be applied. Until now, the influence of these correction terms on the simulated climate variability was not yet understood. Recently, a newly developed GCM without flux correction simulates a reasonably realistic climate without drift [*Boville and Gent,* 1998].

The above mentioned studies with simple and more complex models showed no consensus on the mechanisms and strength of oceanic and atmospheric variability on decadal and interannual timescales. While, for example, *Manabe and Stouffer* [1996] have shown that the frequency characteristics of the climatic variability in their model follow the red noise spectrum predicted from the theory of *Hasselmann* [1976], such a result does not explain the mechanisms responsible for the existence of preferred multidecadal periods of atmospheric variability, which have been found in time series of observed temperature data [*Lau and Weng,* 1995; *Baliunas et al.,* 1997]. One possible starting point for understanding such preferred modes could be studies on the role of chaotic processes for the atmospheric circulation variability like the work of *Hansen et al.* [1997]. The climate simulations performed by these authors suggested that the interannual climate variability at middle and high latitudes is the result of chaotic processes.

The objective of this study is to quantify hints on natural climate variability by long-term integrations with a climate model of the atmosphere-ocean system of moderate complexity which includes the vertical coupling of the troposphere, stratosphere, and mesosphere. The simplifications used in this model permit fast integrations over thousands of years with low computational costs.

The main focus of the investigation is the determination of dominating spatial and temporal modes of the natural atmospheric variability with the aim of quantifying the natural climate variability on timescales of decades to centuries due to internally generated nonlinear dynamical processes and interactions and improving our understanding of the primary mechanisms behind such a variability.

## 2. Model Description

The model applied in this paper is the three-dimensional climate model of the atmosphere-ocean system of moderate complexity developed at the Obukhov Institute of Atmospheric Physics of the Russian Academy of Sciences and is extensively described by *Petoukhov* [1991] and *Petoukhov et al.* [1998]. It is based on modules for atmospheric, oceanic, sea ice, and land surface processes, linked through fluxes of energy, momentum, and water.

The large-scale, long-term dynamical and thermodynamical atmospheric and oceanic fields are described explicitly, while the synoptic and smaller-scale processes are represented in terms of their statistical characteristics, i.e., second moments which are parameterized by a separate set of equations. As a result of this approach, the model equations can be integrated with a much longer time step than that usually used in complex GCMs. Because of the parameterized interactions at synoptic and smaller scales, the complexity of the model has been reduced, which allows an easier interpretation of the results of extended model integrations over centuries and millennia.

### 2.1. Atmospheric Model

The main aim of this study is the analysis of the nonlinear dynamics of large-scale atmospheric circulation patterns and therefore the atmospheric model component is the crucial part of this climate model.

The main concept of the model is the assumption that the basic features of the evolution of the atmosphere can be expressed in terms of large-scale, long-term fields of the main atmospheric variables with characteristic spatial and temporal scales of $\Delta L > 1000$ km and $\Delta\tau > 10$ days and ensembles of synoptic-scale eddies and waves represented by their $(\Delta L^2, \Delta\tau)$ averaged statistical characteristics. This approach is based on data studies which allow one to separate the synoptic-scale and turbulent processes from the large-scale processes in the temporal and spatial domain [*van der Hoven,* 1957; *Vinnichenko,* 1970; *Mitchell,* 1976].

The model governing equations for $(\Delta L^2, \Delta\tau)$ averaged variables and the ensemble characteristics of synoptic-scale eddies are derived from the following set of primitive equations for the atmosphere. The energy balance equation is written in Boussinesq approximation [see, e.g., *Schneider and Lindzen,* 1977; *van Mieghem,* 1973]:

$$\frac{\partial \rho_0 T}{\partial t} = -\nabla_H \cdot \rho_0 \vec{v}_H T - \frac{\partial \rho w T}{\partial z} + \frac{1}{c_v}(-p\nabla \cdot \vec{v}) + q^T. \quad (1)$$

Here $t$ is time, $c_v$ is specific heat of air at constant volume, $\rho$ is density, $\rho_0 = \rho_{00}\exp(-z/H_{00})$, $H_{00} = RT_{00}/g$, $\rho_{00}$ and $T_{00}$ are constant, $z$ is the height, $\vec{v} = (u, v, w)$ is the velocity vector, $\vec{v_H} = (u, v)$ is the horizontal velocity vector, $T$ is air temperature, and $p$ is air pressure. The term $q^T$ stands for sources and sinks of energy, including fluxes of heat due to shortwave and longwave radiation, due to large-scale condensation and dry and moist convection, and due to small-scale and mesoscale turbulence including vertical mixing due to dry/moist convection.

The Reynolds equations for the dynamical atmospheric variables in Boussinesq approximation [see, e.g., *Schneider and Lindzen,* 1977; *van Mieghem,* 1973] are

$$\frac{\partial \rho_0 u}{\partial t} = -\nabla_H \cdot \rho_0 \vec{v}_H u - \frac{\partial \rho w u}{\partial z} - \nabla_\lambda p + f\rho_0 v + \frac{\rho_0 uv}{a}\tan\phi + F_\lambda, \quad (2)$$

$$\frac{\partial \rho_0 v}{\partial t} = -\nabla_H \cdot \rho_0 \vec{v}_H v - \frac{\partial \rho w v}{\partial z} - \nabla_\phi p - f\rho_0 u + \frac{\rho_0 u^2}{a}\tan\phi + F_\phi. \quad (3)$$

Here $f = 2\omega\sin\phi$ is the Coriolis parameter, $\nabla_\lambda p = \partial p/a\cos\phi\partial\lambda$, $\nabla_\phi p = \partial p/a\partial\phi$, and $F_\lambda$ and $F_\phi$ are the $\lambda$ and $\phi$ components of the small-scale and mesoscale (including convective) turbulent friction force $\vec{F}$, correspondingly. The equation for the vertical velocity component is reduced to the hydrostatic balance equation:

$$\frac{\partial p}{\partial z} = -\rho g, \quad (4)$$

where $g$ is the acceleration due to gravity.

The balance equation for water vapor is written in terms of specific humidity $q_v$:

$$\frac{\partial \rho_0 q_v}{\partial t} = -\nabla_H \cdot \rho_0 \vec{v}_H q_v - \frac{\partial \rho w q_v}{\partial z} + q^v, \quad (5)$$

where $q^v$ summarizes sources and sinks of atmospheric water vapor including water vapor flux due to large-scale and moist convection condensation and water vapor flux caused by small-scale and mesoscale turbulent moisture flux.

The set of primitive equations is completed by the continuity equation conventionally used for the description of long-term, large-scale atmospheric processes,

$$\nabla_H \cdot \rho_0 \vec{v}_H + \frac{\partial \rho w}{\partial z} = 0, \quad (6)$$

and by the equation of state,

$$p = \rho R T, \quad (7)$$

where $R$ is the gas constant of the air.

In order to achieve the model governing equations the separation of each variable $y_i$ into a large-scale, long-term $(\Delta L^2, \Delta\tau)$-averaged component, $\widehat{y_i}$, and a synoptic-scale deviation, $y_i'$, is applied to the above described set of primitive equations (1)-(7), i.e.,

$$y_i = \widehat{y_i}(\lambda, \phi, z, t) + y_i'(\lambda, \phi, z, t), \quad (8)$$

where the synoptic component is approximated by an incompressible fluid $\nabla \cdot \vec{v}' = 0$.

The equations (1)-(7) are subjected then to $(\Delta L^2, \Delta\tau)$-averaging. As a result, the averaged equations include, besides large-scale, long-term components $\widehat{y_i}$, the second moments of synoptical component $\widehat{y_i' y_j'}$.

In order to illustrate the applied procedure, the $(\Delta L^2, \Delta\tau)$-averaged energy equation describing the temporal evolution of the large-scale temperature is shown:

$$\frac{\partial \rho_0 \widehat{T}}{\partial t} = -\nabla_H \cdot (\rho_0 \widehat{T}\widehat{\vec{v_G}} + \rho_0 \widehat{T}\widehat{\vec{v_a}}) - \nabla_H \cdot (\rho_0 \widehat{T'\vec{v}_H'}) - \nabla_z(\widehat{\rho}\widehat{T}\widehat{w}) - \nabla_z(\widehat{\rho}\widehat{T'w'} + \widehat{T}\widehat{\rho' w'} + \widehat{w}\widehat{\rho' T'}) - \frac{1}{c_v}\widehat{p}\nabla \cdot \widehat{\vec{v}} + \widehat{q^T}. \quad (9)$$

The large-scale horizontal wind vector $\widehat{\vec{v_H}} = (\widehat{u}, \widehat{v})$ is divided additionally into geostrophic and ageostrophic components:

$$\widehat{\vec{v_H}} = \widehat{\vec{v_G}} + \widehat{\vec{v_a}}. \quad (10)$$

The geostrophic velocity components are described using the thermal wind approximation. The large-scale dynamical fields are assumed to adapt instantaneously to the thermal fields.

The second moments of synoptical components are governed in the model by a separate set of equations derived by *Petoukhov* [1991] from the primitive equations by applying the commonly used procedure in statistical fluid mechanics and the theory of turbulence [*Kraichnan,* 1962]. Additionally, the synoptic-scale components are assumed to be statistical ensembles, which are quasi-geostrophic in the free atmosphere and Gaussian in space and time with spatial and temporal correlation radii less than $\Delta L$ and $\Delta\tau$, respectively. Besides, the vertical synoptic-scale second moments, $\widehat{w' y_i'}$, are assumed to adapt instantaneously to the large-scale component and to the other synoptical second moments. The assumption on the Gaussian type of the synoptic processes allows one to omit all odd moments and to express all even moments in terms of the second moments. As an example, to obtain the equation for the zonal atmospheric heat flux $\widehat{u'T'}$, the primitive equations for zonal velocity (equation (2)) and temperature (equation (1)) are multiplied, by $T'$ and $u'$, respectively. The resultant equations are combined then and subjected to the above mentioned $(\Delta L^2, \Delta\tau)$ spatial and temporal averaging, which yields

$$\rho_0\frac{\partial\widehat{u'T'}}{\partial t} = -\rho_0\widehat{u'\vec{v}_H'}\cdot\nabla_H\widehat{T} - \rho_0\widehat{T'\vec{v}_H'}\cdot\nabla_H\widehat{u} - \rho_0\widehat{\vec{v}_H}\cdot\nabla_H\widehat{T'u'} - \widehat{\rho}\widehat{u'w'}\nabla_z\widehat{T} - \widehat{\rho}\widehat{T'w'}\nabla_z\widehat{u} - \widehat{\rho}\widehat{w}\nabla_z\widehat{u'T'} + \widehat{u'T'}\nabla_z\widehat{\rho'w'} + \frac{\rho_0}{a}\tan\phi(\widehat{u}\widehat{v'T'} + \widehat{v}\widehat{u'T'}) + \widehat{q_D^{uT}} - \frac{1}{c_v}\widehat{u'p'}\nabla\cdot\widehat{\vec{v}} + \widehat{q_T^{uT}}. \quad (11)$$

The term $\widehat{q_D^{uT}}$ describes the diabatic contribution due to radiation, large-scale condensation, and moist convection. The small-scale turbulent diffusion $\widehat{q_T^{uT}}$ of $\widehat{u'T'}$ is parameterized in equation (11) as

$$\widehat{q_T^{uT}} = \nabla_H K_H\rho_0\nabla_H\widehat{u'T'} + \nabla_z K_z\widehat{\rho}\nabla_z\widehat{u'T'}.$$

$K_H$ and $K_z$ are the small-scale horizontal and vertical exchange coefficients, respectively.

The same procedure is used to derive equations for any other $\widehat{y_i'y_j'}$. For instance, the equation for the zonal component $\widehat{u'^2}$ of the synoptic-scale kinetic energy is obtained by multiplying equation (2)with $u'$ and applying then the $(\Delta L^2, \Delta\tau)$-averaging. In order to close the set of equations, the following second moments are required: $\widehat{u'^2}$, $\widehat{v'^2}$, $\widehat{u'T'}$, $\widehat{v'T'}$, $\widehat{u'q_v'}$, $\widehat{v'q_v'}$, $\widehat{u'v'}$, $\widehat{T'^2}$, $\widehat{q_v'^2}$, $\widehat{T'q_v'}$, $\widehat{u'w'}$, $\widehat{v'w'}$, $\widehat{T'w'}$, $\widehat{q_v'w'}$, $\widehat{\rho'w'}$, and $\widehat{w'^2}$. Model equations (9) and (11) show that the temporal evolution of the large-scale temperature pattern is determined by the zonal, meridional, and vertical heat fluxes due to synoptic-scale disturbances and vice versa.

In the work of *Petoukhov* [1991] a scale analysis was applied to the equations for the large-scale, long-term components and second synoptic moments, distinguishing between tropics and extratropics and between planctary boundary layer and free atmosphere. For example, equation (11) for the evolution of synoptic zonal heat flux in the free troposphere of temperate latitudes is reduced to

$$\rho_0\frac{\partial\widehat{u'T'}}{\partial t} = -\rho_0\widehat{u}\nabla_\lambda\widehat{u'T'} - \rho_0\widehat{v}\nabla_\phi\widehat{u'T'} - \rho_0\widehat{u'^2}\nabla_\lambda\widehat{T} + \widehat{u'T'}\nabla_z\widehat{\rho'w'} + \nabla_H(K_H\rho_0\nabla_H\widehat{u'T'}) + \nabla_z(K_z\rho_0\nabla_z\widehat{u'T'}). \quad (12)$$

Neglecting the barotropic component compared to the baroclinic one of the synoptic-scale ensemble generation, the equation for $\widehat{u'^2}$ entering the right-hand side of equation (12) is as follows:

$$\rho_0\frac{\partial\widehat{u'^2}}{\partial t} = -\rho_0\widehat{u}\nabla_\lambda\widehat{u'^2} - \rho_0\widehat{v}\nabla_\phi\widehat{u'^2} - 2\rho_0\widehat{u'w'}\nabla_z\widehat{u} + \widehat{u'^2}\nabla_z\widehat{\rho'w'} + 2\nabla_H(K_H\rho_0\nabla_H\widehat{u'^2}) + 2\nabla_z(K_z\rho_0\nabla_z\widehat{u'^2}). \quad (13)$$

By the usage of the hydrostatic balance equation (4) multiplied with $w'$ and subjected to the $(\Delta L^2, \Delta\tau)$-averaging, the equation for $\widehat{\rho'w'}$ entering equations (12) and (13) can be written in the form

$$R\widehat{T}\nabla_z\widehat{\rho'w'} + (g + R\nabla_z\widehat{T})\widehat{\rho'w'} + R\widehat{T'w'}\nabla_z\widehat{\rho} + R\widehat{\rho}\nabla_z\widehat{T'w'} = 0. \quad (14)$$

The $\widehat{u'w'}$ and $\widehat{T'w'}$ moments are described by the following set of equations:

$$\rho_0\widehat{w'^2}\nabla_z\widehat{u} = \widehat{u'w'}\nabla_z\widehat{\rho'w'} + \nabla_H K_H\rho_0\nabla_H\widehat{u'w'} + \nabla_z K_z\rho_0\nabla_z\widehat{u'w'}, \quad (15)$$

$$\rho\widehat{w'^2}\nabla_z\widehat{T} = \widehat{T'w'}\nabla_z\widehat{\rho'w'} + \nabla_H K_H\rho_0\nabla_H\widehat{T'w'} + \nabla_z K_z\rho_0\nabla_z\widehat{T'w'}. \quad (16)$$

Equations (15) and (16) are obtained by *Petoukhov* [1991] by multiplication of equation (2) and (1) with $w'$ and subsequent $(\Delta L^2, \Delta\tau)$-averaging.

The autocorrelation function $\widehat{w'^2}$ of the synoptic ensemble vertical velocity enters equations (15) and (16). An equation for this variable is derived by *Petoukhov* [1991] from the pressure tendency equation multiplied by $w'$ and $(\Delta L^2, \Delta\tau)$-averaged and follows as

$$\widehat{\rho}g\widehat{w'^2} = -R\left(\nabla_H K_H\rho_0\nabla_H\widehat{T'w'} + \nabla_z K_z\widehat{\rho}\nabla_z\widehat{T'w'}\right) + \widehat{w'\vec{v}_H'}\cdot\nabla_H\widehat{p} - \widehat{w}g\widehat{\rho'w'}. \quad (17)$$

The second moments $\widehat{w'^2}$ and $\widehat{\rho'w'}$ are expressed as functions of the mean gradients:

$$\widehat{w'^2} = A_{w2}\left(\frac{\widehat{\rho'w'}}{\rho_0}\right)^2\left[\frac{A_g g}{R\Gamma}\left(1 - \frac{T_H}{T_{00}}\right) - 1\right], \quad (18)$$

$$\widehat{\rho'w'} = A_{\rho w}H_{00}\rho_0\left[\left(\frac{\partial\widehat{u}}{\partial z}\right)^2 + \left(\frac{\partial\widehat{v}}{\partial z}\right)^2\right]^{1/2} \times\left[\left(\frac{\nabla_\lambda\widehat{p(0)}}{\rho(0)g}\right)^2 + \left(\frac{\nabla_\phi\widehat{p(0)}}{\rho(0)g}\right)^2\right]^{1/2}, \quad (19)$$

where $A_{\rho w} = \sqrt{2}$, $A_{w2} = 1/(2\sqrt{2})$, and $A_g = \sqrt{2}$ are disposable parameters and $\Gamma$ is the temperature lapse rate of the free troposphere [*Petoukhov*, 1991].

In deriving the final set of model equations it was further assumed that the $(\Delta L^2, \Delta\tau)$-averaged scales of the atmosphere have a universal vertical structure of temperature and humidity fields. This allows the derivation of vertically averaged prognostic equations for temperature and water vapor without specific vertical resolution. Thus the vertical structure of the large-scale, long-term component of the atmosphere can be represented by several basic layers. These layers have sta-

ble structural features under a broad range of climatic states, even somewhat away from present-day climate conditions.

The model atmosphere is represented by the surface layer, planetary boundary layer, free troposphere, and several stratospheric layers ($H_{tr} < z < 25$ km, 25 km $< z <$ 47 km, 47 $< z <$ 60 km, 60 $< z <$ 70 km, and 70 $< z <$ 80 km, where $H_{tr}$ is the tropopause height) in which large-scale, long-term atmospheric variables exhibit substantially different vertical distributions. The vertical temperature profiles, $T(z)$, inside the free troposphere and stratospheric layers are considered to be linear [*Khrgian,* 1978; *Andrews et al.,* 1987; *Gulev et al.,* 1991]; the vertical distribution of the specific humidity, $q_v(z)$, in the free atmosphere is supposed to be exponential [*Saltzman and Vernekar,* 1971; *Khrgian,* 1978]. In the surface layer at high and middle latitudes the atmospheric variables in the model are described according to Monin-Obukhov similarity theory [*Deardorff,* 1968]. In the remaining part of the planetary boundary layer a modified Ekman formulation has been used [e.g., *Hansen et al.,* 1983]. In the tropical region the Ekman model is generalized by accounting for the vertical advection and horizontal turbulent diffusion of heat, moisture, and momentum [*Petoukhov and Ganopolski,* 1994].

To obtain the governing model equations for the troposphere, the nonstationary equations for large-scale, long-term components and for the synoptic-scale moments are integrated over the total tropospheric column. In so doing, the vertical structure of the $\widehat{u'T'}$ and $\widehat{v'T'}$ moments is described using the parameterization proposed by *Petoukhov* [1980], which is close to the *Nakamura et al.* [1994] description, while the vertical profile of $\widehat{u'q'_v}$ and $\widehat{v'q'_v}$ is supposed to damp exponentially [*Petoukhov et al.,* 1998].

The same integration procedure is applied to all equations in the above mentioned stratospheric layers. For this reason the vertical profiles of all synoptic moments in the stratosphere of high and middle latitudes are assigned in accordance with the Charney-Drazin theory [*Charney and Drazin,* 1961] modified by taking into account the gravity wave drag, Newtonian cooling, and Rayleigh friction as described by *Petoukhov et al.* [1998].

The diabatic heating rates are determined by including shortwave and longwave radiation, large-scale precipitation and condensation, moist cumulus convection and small-scale turbulent fluxes of momentum, and sensible and latent heat [*Petoukhov et al.,* 1998]. The integration of the nonstationary equations with height, expansion of horizontal velocity field into thermal wind and nonthermal wind components, as well as the statistical description of synoptic components in terms of second moments allow one to use a comparatively large time step between 1 and 5 days without violation of the stability criterion when numerically solving the prognostic equations of the model.

### 2.2. Oceanic Model

The basic equations of the model for the long-term, large-scale component and for the synoptic-scale component of the ocean processes are deduced from the set of primitive equations using the same $(\Delta L^2, \Delta\tau)$ averaging as that in the atmosphere and scale analysis [*Petoukhov,* 1991]. The equations for the oceanic second moments are obtained using the same method as that in the atmospheric model, whereby in the oceanic part all synoptic-scale fluxes are parameterized in a stationary manner.

The mentioned equations are considered in the model separately in typical oceanic regions: open ocean with subdivision of seasonal/main thermocline, mixed layer, bottom layer, and littoral ocean with the same vertical subdivision. All these regions are considered outside the tropical belt and within it.

The important assumption used in the derivation of the model governing equations for the ocean is the supposition on a universal vertical structure of temperature and salinity fields in the above mentioned vertical layers. The temperature profile is supposed to be isothermal in the mixed layer, self similar in the seasonal thermocline, Needler-type in the main thermocline, and self similar in the bottom layer.

To obtain the governing equations of the ocean model, the basic equations are integrated in the model with respect to depth in the limits of the described vertical layers. This procedure gives the final nonstationary equations of the oceanic model for temperature in the mixed layer and in the seasonal and the main thermoclines. Dynamic fields in the model ocean are described in a stationary approximation. Oceanic salinity currently is prescribed regarding its spatial distribution and annual cycle according to *Stepanov* [1974]. The reason for this prescription is the lack of adequate models for the continental runoff to different regions of the oceanic basins as well as the low reliability of correspondent empirical data.

### 2.3. Land Processes and Sea Ice Model

The interaction among the atmosphere, ocean, land, and ice surfaces occurs through the fluxes of momentum, energy, and water vapor. The calculation of this interaction is based on the Biosphere-Atmosphere Transfer Scheme (BATS) by *Dickinson et al.* [1986]. In detail, the model employs similar surface types, soil texture and color classes, and calculation of surface albedo to those in the BATS scheme. Vegetation fraction in each grid cell is a function of soil temperature, which is determined by solving the heat balance equation of the underlying surface. The soil moisture is represented by a two-layer model. Surface fluxes of momentum, energy, and water vapor are computed by using the conventional bulk formulas, whereas the surface roughness is calculated by combining the surface roughness for a given surface type and orographical roughness depending on explicitly specified large-scale orography.

The sea ice model is based on that described by *Bryan* [1969]. An equation for the temporal evolution of sea ice thickness has been solved under the influence of large-scale and synoptic-scale atmospheric and oceanic components. Again, the synoptic-scale advective terms are parameterized as described by *Petoukhov* [1991].

### 2.4. Current Model Version

It should be noticed here that in the current version of the model employed for this study the prognostic equations are used only for atmospheric temperatures, for the second moments $\widehat{u'^2}$, $\widehat{v'^2}$, $\widehat{u'T'}$, and $\widehat{v'T'}$, and for mixed layer and seasonal/main thermocline temperatures, while all other large-scale variables and synoptic second moments are treated in a diagnostic approximation. In section 4.2 we discuss the influence of the stationary and nonstationary parameterization of meridional and zonal heat fluxes $\widehat{u'T'}$ and $\widehat{v'T'}$ and of the horizontal components $\widehat{u'^2}$ and $\widehat{v'^2}$ of the synoptic-scale kinetic energy on the results of the model runs.

Soil color and texture and vegetation characteristics (e.g., vegetation/land cover types, roughness, and albedo) are assigned to their present-day climate spatial and temporal (annual cycle) distributions. Sea ice thickness is a function of the oceanic mixed layer temperature and of the surface air temperature. These simplifications, on the one hand, put rather rigorous limitations on the number of feedbacks in the model operating in comparison to the real climate system, but on the other hand, they allow one to get a clearer picture as to the most important possible mechanisms responsible for decadal climate variability in the model. Currently, we can only speculate on the contribution of the neglected processes to the modeled variability. Since the results of *Slonovsky et al.* [1997] show a strong correlation between winter sea ice concentration and winter sea level pressure changes on the decadal timescale, a nonstationary sea ice scheme will be involved in future long-term simulations. The main dynamical and physical features of the current version of the climate model are summarized in Table 1 and Table 2.

## 3. Model Climatology

In order to assess the reliability of the climate model, in this section we describe the performance of the model as to the model climatology and to some aspects of the model variability. For the first purpose we portrayed selected variables in the latitude-height meridional section as well as in geographical distribution. These zonal and geographical distributions have been obtained by integrating the model over 60 years and averaging over the last 10 model years. Notice here that the comparison of the model results after 60 years of integrations with those ones after 1000 years of integrations reveals no substantial drift in the model climate characteristics.

Figure 1 shows the zonally averaged temperature distribution for January and July conditions. The agreement between the simulated and observed temperature structures up to 80 km height [see *Andrews et al.*, 1987] is reasonably good. The model reproduces the strength and extension of the polar vortex over the Arctic and Antarctic quite well.

The zonal mean zonal wind distributions are displayed for January and July in Figure 2. These distributions show the well-known west wind structures over the winter hemisphere and east wind jets over the summer hemisphere at stratospheric and mesospheric heights. Compared to the observations shown by *Andrews et al.* [1987], some differences can be found in January; that is, the northern jet velocity is up to 10-20 m/s larger than the observations, and there is a slight poleward shift of the jet core. The southern jet velocity is too weak by 10 m/s. In the troposphere the subtropical jets are simulated by the model at about $40^o$ with jet velocities similar to observations. However, in the Northern Hemisphere the northward shifting of the jet axis from January to July is not pronounced, whereas

**Table 1.** Main Dynamical Features of the Current Version of the Climate model

| Model Characteristic | Current Model State |
|---|---|
| Spatial resolution | Horizontal: $6^o$longitude $\times$ $4.5^o$ latitude; vertical: 8 layers in atmospheric module (18 layers for radiative transfer); 3 layers in oceanic module; 2 layers in land module |
| Time step | 1 to 5 days |
| Basic equations | prognostic equations for atmospheric and oceanic temperature; diagnostic equations for atmospheric and oceanic large-scale, long-term circulation patterns, specific humidity, sea ice thickness, and soil moisture; prognostic equations for atmospheric moments of $\widehat{u'T'}$, $\widehat{v'T'}$, $\widehat{u'^2}$, and $\widehat{v'^2}$; diagnostic equations for all other atmospheric and oceanic synoptic components; energy balance equations for temperatures of land and sea ice surface |
| Prescribed parameters | optical parameters of atmospheric gases, water droplets, and aerosols in solar and terrestrial radiation bands; aerosols' and greenhouse gases' concentrations; horizontal small-scale/mesoscale eddy coefficients for momentum, heat,and moisture; spatial distributions of soil and vegetation parameters; oceanic salinity in all layers in seasonal course |

**Table 2.** Main Physical Features of the Current Version of the Climate Model

| Component/Process | Main Physical Features |
|---|---|
| Atmosphere | radiative transfer; large-scale circulation; synoptic-scale eddy horizontal/vertical transport of momentum, heat, and moisture; small-scale/mesoscale turbulent diffusion; large-scale condensation and moist convection |
| Ocean | large-scale horizontal and vertical momentum and heat exchange; synoptic scale eddies, convection, and small-scale/mesoscale diffusion |
| Land | soil/vegetation/atmosphere momentum, heat, and moisture exchange |
| Explicit temperature-related feedbacks | water vapor; snow/ice albedo; cloudiness; lapse rate; horizontal/vertical transport processes in the atmosphere and ocean |
| Surface types | 16 vegetation and land cover and soil types (with/without snow cover); open ocean; inland water; sea ice; Antarctic/Greenland ice sheets |
| Explicitly resolved orography | Plateaus of Tibet and Iran, Altai, Ural Mountains, Alps, Carpathians, Rocky Mountains, Andes, Atlas Mountains, Drakensberg, Ethiopian Plateaus, Great Dividing Range, and Antarctic and Greenland Sheets |
| Radiation | $H_2O$, $O_3$, $CO_2$ (longwave), aerosol (shortwave), and effective one-layer cloudiness (low/middle layer stratus and cumuli with corresponding cloud amounts) |

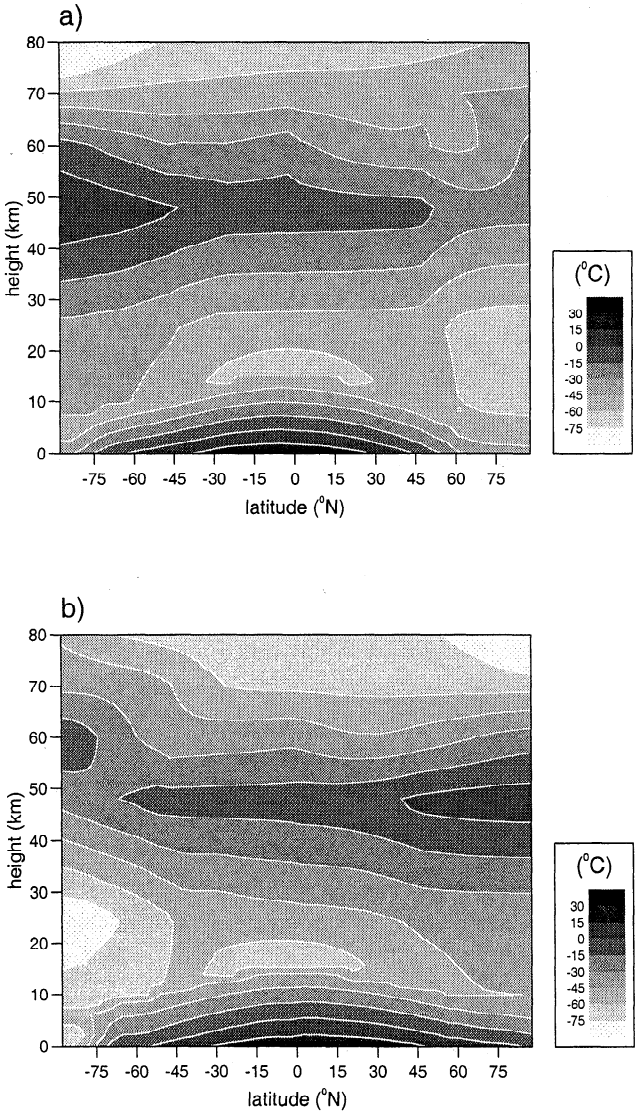


**Figure 1.** Mean zonally averaged temperature, averaged over years 50-60 of the coupled model run, in (a) January and (b) July. Temperatures are shown from 0 to 80 km height and from 87.5°S to 87.5°N.

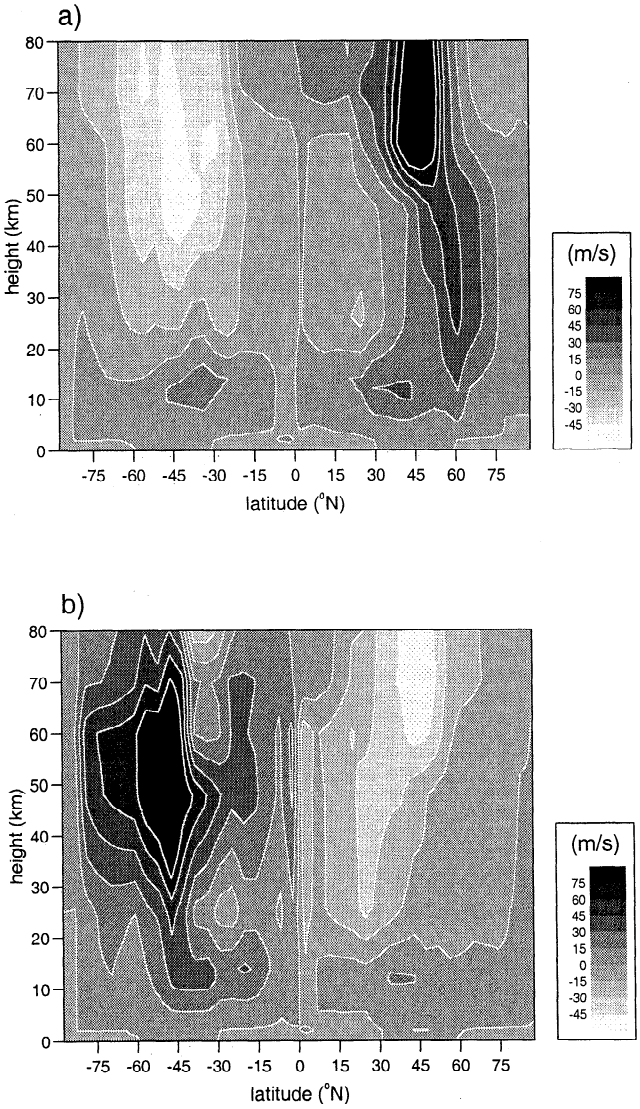


**Figure 2.** Mean zonally averaged zonal wind, averaged over years 50-60 of the coupled model run, in (a) January and (b) July. Zonal winds are shown from 0 to 80 km height and from 87.5°S to 87.5°N.

in the Southern Hemisphere under July conditions there is no clear distinction between the tropospheric jet and the area of large velocities extended from mesospheric and stratospheric heights down to tropospheric heights. The zonally averaged meridional wind distribution not presented here shows the observed structure of three circulation cells in the troposphere and the interhemispheric circulation exchange in the stratosphere and mesosphere.

Figure 3, Figure 4, and Figure 5 portray the geographical distributions of monthly averaged surface air temperature (SAT), sea level pressure (SLP), and precipitation in comparison to observations. The observational data are climatological averages of SAT, SLP, and precipitation over the period 1950-1979 between $45^0$S and $90^0$N provided by *Shea et al.* [1994]. The geographical distributions of SAT (Figure 3) show a principal coincidence between modeled and observed temperatures. The main differences occur owing to the too weak oceanic currents, which are possibly caused by the prescribed salinity. Some smaller differences can be explained by the rather coarse description of orography (e.g., temperatures over the Tibetan Plateau).

The comparison of the observed sea level pressure with that simulated by the model (Figure 4) reveals that the model satisfactorily describes the strength and location of the large-scale characteristic pressure patterns of the Northern Hemisphere. This includes the subtropical high-pressure areas over the Atlantic (Azores high) and over the Pacific, the subpolar low-pressure areas (Iceland low and Aleutian low), and the cold Siberian high in January. Differences appear according to the strength of some of the pressure centers, which is too large for the subtropical high-pressure centers and too weak for the Iceland low. Furthermore, during January conditions a rather unrealistic high-pressure area near the Great Lakes is simulated. In July the Aleutian low is much more pronounced in the model than in observa-

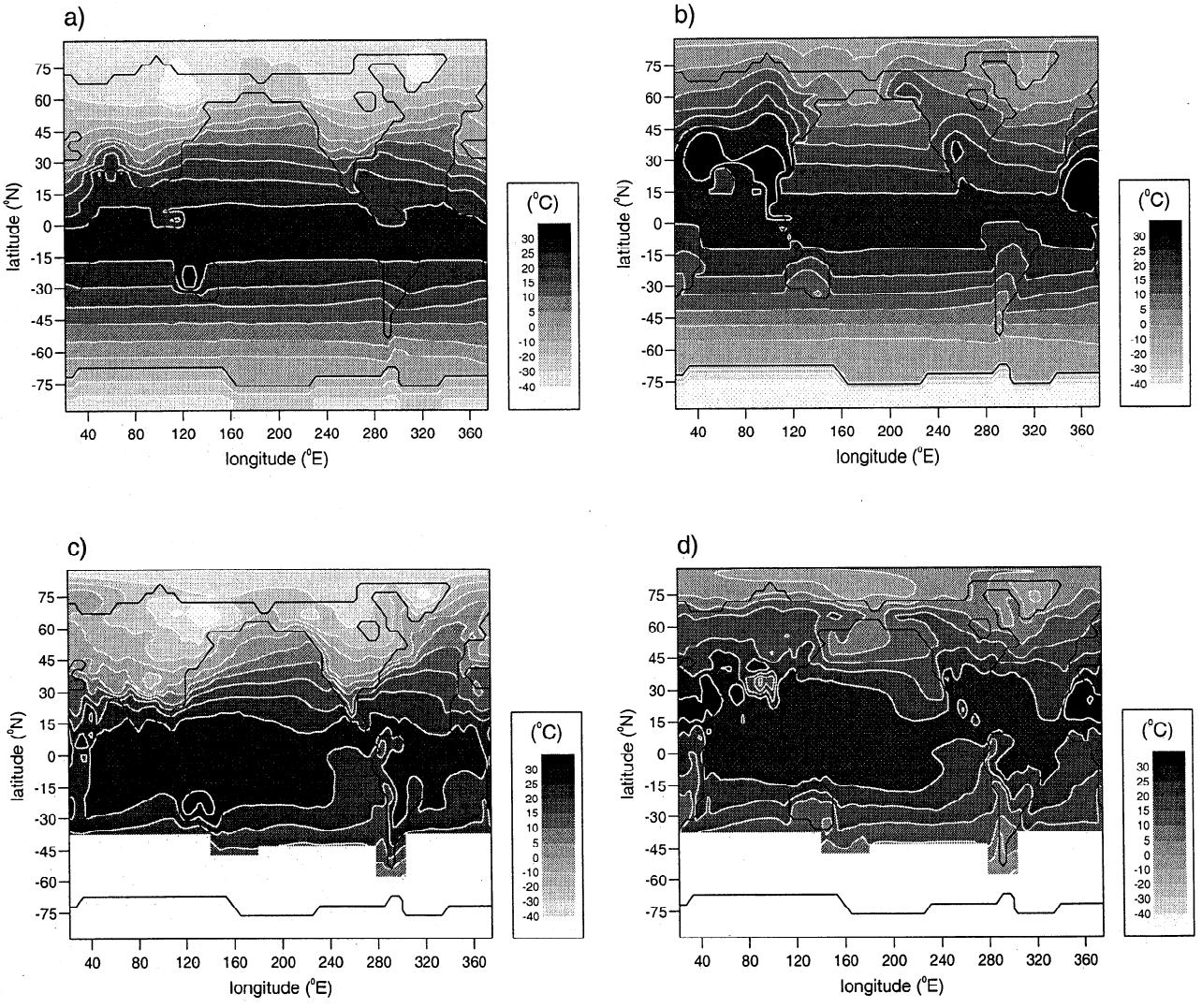


**Figure 3.** Mean surface air temperature, averaged over years 50-60 of the coupled model run, in (a) January and (b) July. For comparison, climatological observations according to *Shea et al.* [1994], averaged over the period 1950-1979, are shown for (c) January and (d) July.

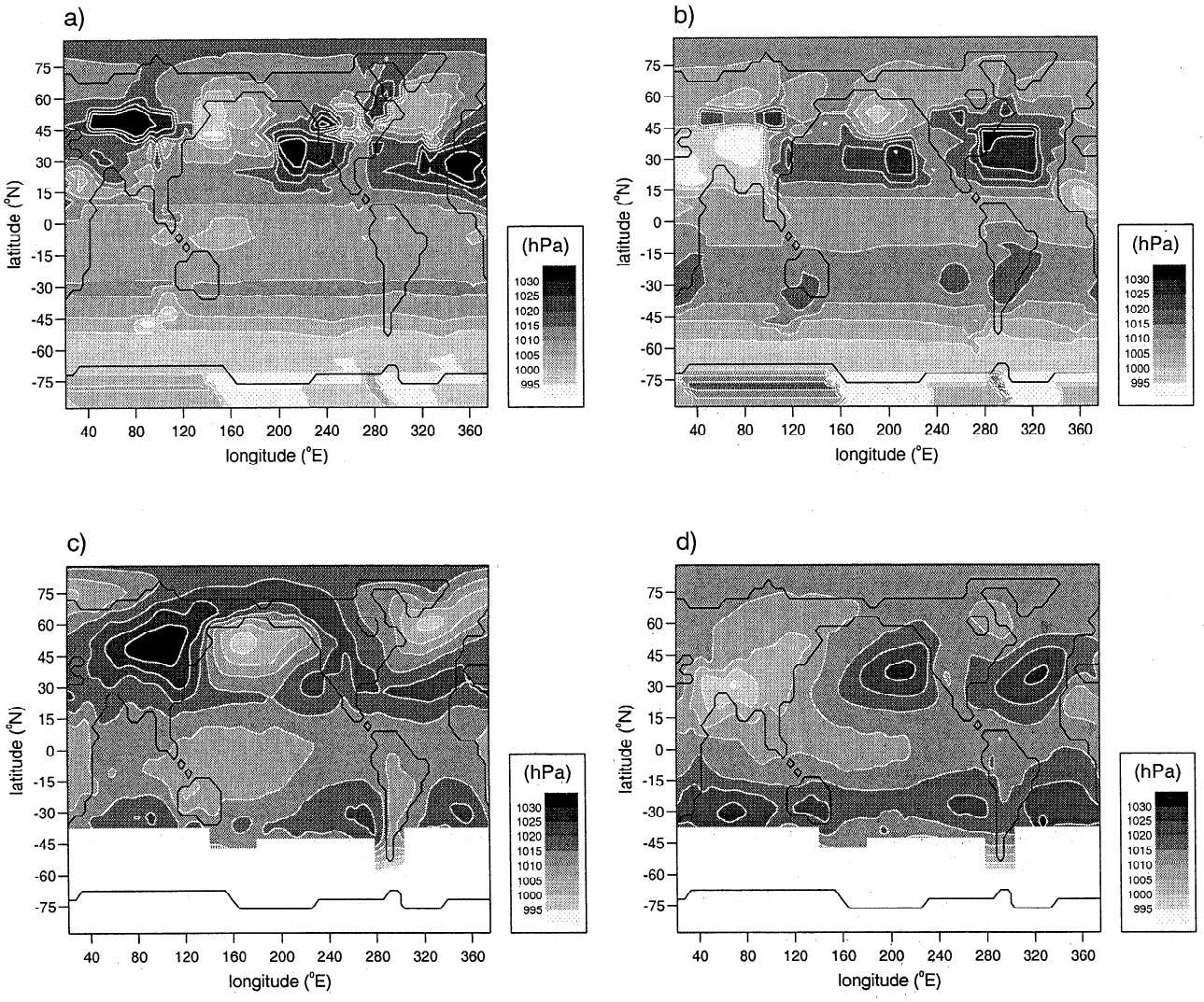


**Figure 4.** Mean sea level pressure averaged over years 50-60 of the coupled model run, in (a) January and (b) July. For comparison, climatological observations according to *Shea et al.* [1994], averaged over the period 1950-1979, are shown for (c) January and (d) July.

tions, and the center of the Azores high is shifted too far west. In the Southern Hemisphere in January, instead of the three observed cells of high pressure, a band of increased pressure is simulated at the correct latitudes but with too low central pressure. In July the observed four-cell structure of the subtropical high-pressure areas is captured by the model; again the strength is too weak. The positions of the high-pressure areas at the east coasts of the continents are modeled too far westward, whereas the position of the other highs is reasonably well represented. To sum up, we can conclude that the acceptable description of large-scale characteristic pressure patterns gives rise to the assumption that the model can reproduce the centers of the well-known teleconnection patterns of the Northern Hemisphere, for example, of the North Atlantic Oscillation (NAO).

The model validation presented here includes the comparison between observed and simulated precipitation (Figure 5) because this distribution influences the large-scale atmospheric circulation by latent heat release. There is a fairly satisfactory agreement between the observed and simulated patterns but with smaller simulated precipitation rates. Mainly, this can be recognized in the tropical regions where the extension of the areas with very high values of precipitation is smaller in the simulation. At the west coasts of the American and African continents areas with very low precipitation rates are more pronounced in the model results.

In order to elucidate the similar structures of observed and modeled atmospheric circulation, we have presented different modeled fields and their observational counterparts. An inspection of the difference fields between simulations and observations (not shown) reveals a somewhat larger but similar error range compared to those obtained by *Gates et al.*, [1999] for the comparison of the ensemble means of 31 GCMs with

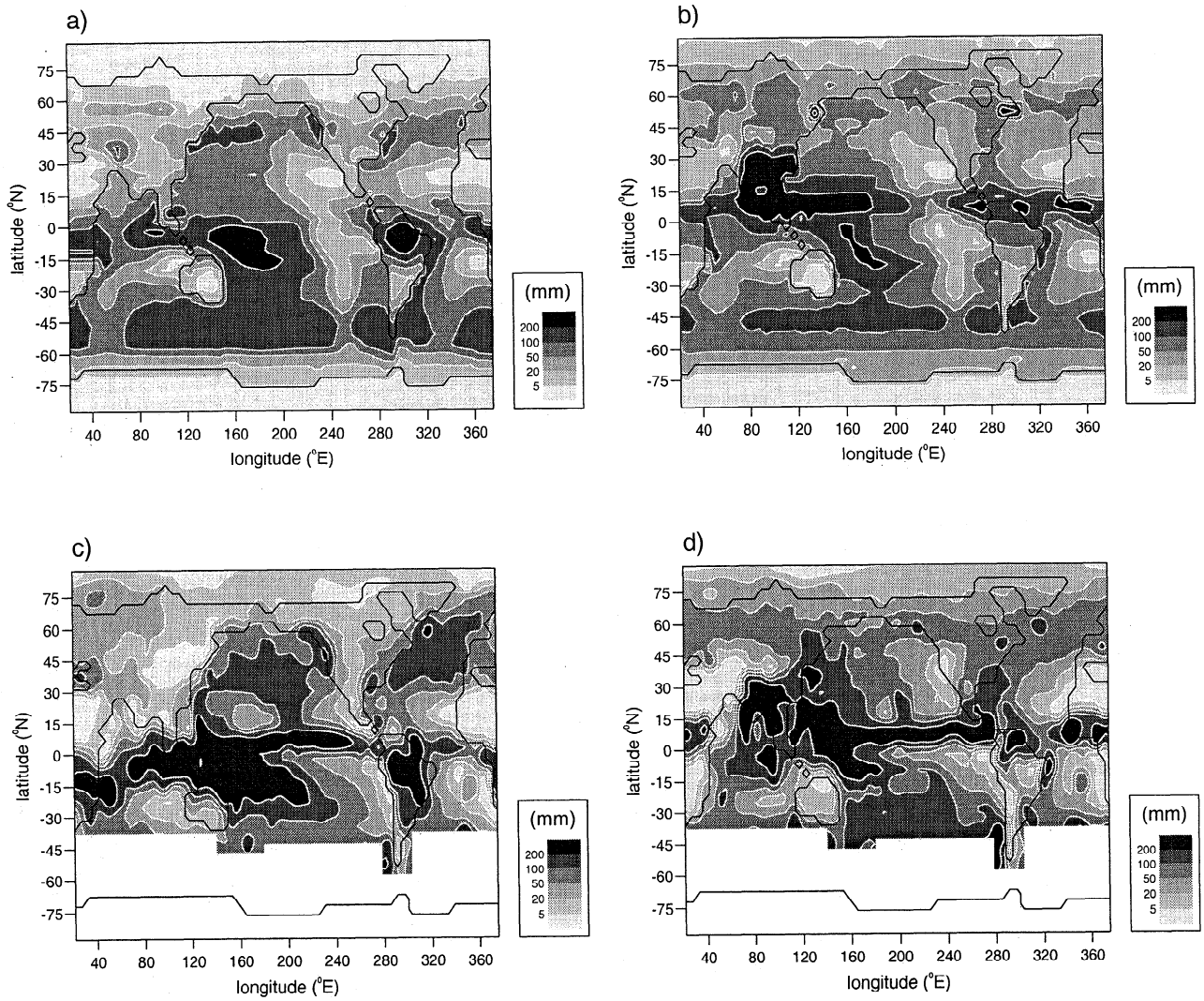


**Figure 5.** Mean precipitation averaged over years 50-60 of the coupled model run, in (a) January and (b) July. For comparison, climatological observations according to *Shea et al.* [1994], averaged over the period 1950-1979, are shown for (c) January and (d) July.

European Centre for Medium-Range Weather Forecasts (ECMWF) reanalysis (Atmospheric Model Intercomparison Project I (AMIP I)).

A more extended analysis of present-day climate simulations of our global climate model is presented by *Petoukhov et al.,* [1998] including additional zonal and geographical distributions of the annual mean and annual cycle characteristics for several fields in the atmosphere and ocean. Together with the analysis of the annual cycle, this model has been tested to reproduce the intraseasonal and interannual temperature variability, particularly the quasi-biennial oscillations, in comparison to observations [*Eliseev et al.,* 1997; *Mokhov et al.,* 1997, 1998]. According to *Mokhov et al.* [1998], the model simulates quite reasonably the probability density functions for intraseasonal surface air temperature variations in different regions compared with the analysis of the observed daily data during the last century at different locations. As one example to illustrate the variability of the model, we present in Figure 6 the time series of globally and hemispherically averaged annual mean surface air temperature anomalies from the 1000 year long model integration of the coupled atmosphere-ocean model. First, it is confirmed that no model drift occurs at all. Second, the model reveals a considerable variability, the standard deviation of the globally averaged temperature amounts to 0.5 K. Third, in coincidence with observations, the Northern Hemispheric variability (standard deviation of 0.85 K) is much larger than those of the Southern Hemisphere (standard deviation of 0.3 K). A detailed analysis of decadal and interdecadal variability is the main purpose of this study, and in section 4 we present detailed investigations on this topic.

In summary, the model simulates the main large-scale features of atmospheric circulation in satisfactory agreement with observational data and presents an appropriate tool for analyzing the variability of such large-scale atmospheric patterns on decadal and interdecadal timescales.

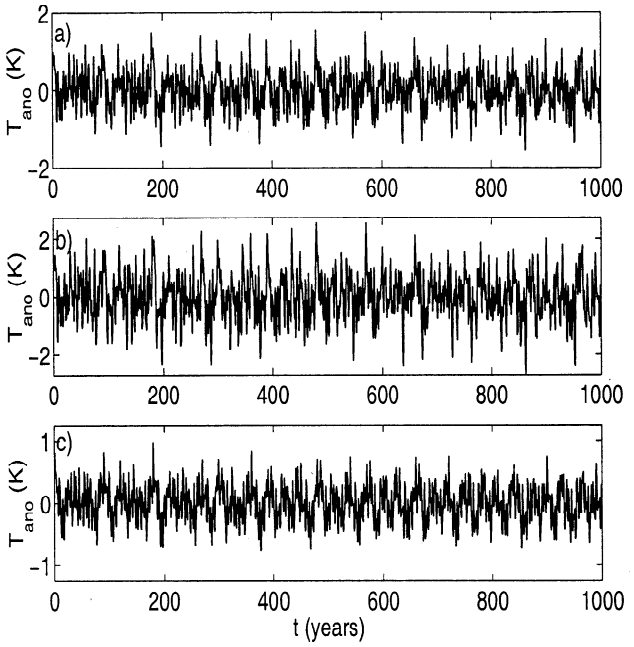


**Figure 6.** Annual time series of anomalies of globally and hemispherically averaged surface air temperature from the 1000 year long integration of the coupled model: (a) globally averaging, (b) averaging over Northern Hemisphere, and (c) averaging over Southern Hemisphere.

## 4. Analyses of Decadal Variability

In order to study the natural variability of the model climate and its causes, the variability of the coupled atmosphere-ocean system and the sea surface temperature (SST) forced atmospheric variability has been determined. This is done by analyzing the spatiotemporal structure of two long-term runs of the above described climate model of moderate complexity with two different presentations of the ocean model (coupled model and fixed SST model with prescribed climatological, seasonally varying SSTs). Our main focus is to understand the causes of the dynamically induced variability in the troposphere and stratosphere of the Northern Hemisphere. In order to emphasize the decadal and interdecadal timescales, annual averaged fields of sea level pressure, of sea surface temperature, and of stream function in geostrophic approximation at 5 km ($\approx$ 500 hPa), 18 km ($\approx$ 70 hPa), and 35 km ($\approx$ 10 hPa) have been investigated. The horizontal resolution amounts to $\Delta\phi = 4.5^o$ and $\Delta\lambda = 6^o$. After a short description of the analyzing methods, results of 1000 year long model runs of the model with interactive ocean and with prescribed SST are presented.

### 4.1. Analyzing Methods

Insight into the spatial and temporal structures of the atmospheric circulation yields the common empirical orthogonal function (EOF) analysis of the fields of various quantities [see, e.g., *Preisendorfer,* 1988]. In the framework of EOF analysis the field of a scalar quantity $\vec{X}$ is projected onto the space spanned by the EOFs:

$$\vec{X} = \sum_{j=1}^{J} \alpha_j(t)\vec{e_j}. \tag{20}$$

Here $\vec{e_j}$, $(j = 1, ..., J)$ are the EOFs representing the spatial patterns for our data sets and $J$ is their total number. The time-dependent amplitude $\alpha_j(t)$ of $\vec{e_j}$ is called the $j$th principal component (PCj) of the time series. The EOFs are computed as the eigenvectors $\vec{e_j}$ of the covariance matrix of the field $\vec{X}$. For the calculation of all EOFs and PCs presented in this study we used a normalization given by *Werner and von Storch* [1993] by which the time series of the PC has the variance one and the EOF pattern shows the relative strength of the signal.

In order to determine the dominant temporal scales of the analyzed meteorological fields as well as their local temporal changes, the time series of principal components or of meteorological values at single grid points have been subjected to a continuous wavelet transformation. This method [see, e.g., *Kumar and Foufoula-Georgiou,* 1997] was introduced in order to overcome the limited time-frequency localization of the Fourier transformation for multiscale, nonstationary signals and it is a well-suited tool for climate signal detection [e.g., *Lau and Weng,* 1995]. In contrast to the common Fourier methods, the wavelet method transforms a given time series to a scale-time domain. This is done by correlation of the time series $f$ with stretched and translated local base functions $\Psi$ $(a, b \in \mathbf{R},\ a > 0)$:

$$\begin{aligned} T(a,b) &= \int_{-\infty}^{\infty} f(t)\,\overline{\Psi_{a,b}(t)}\,dt \\ &= \frac{1}{a^{1/2}} \int_{-\infty}^{\infty} f(t)\,\overline{\Psi(\frac{t-b}{a})}\,dt. \end{aligned} \tag{21}$$

The function $\Psi$ is called a wavelet and presents a function with limited energy and with a zero mean. The wavelet coefficients $T(a, b)$ provide information about the scale $a$ (inverse proportional to the frequency) as well as about the time $b$ of appearance of a characteristic structure, and therefore they allow the detection of local temporal changes in the spectral distribution of energy.

Furthermore, the time series $f$ can be recovered from its wavelet transform $T(a, b)$ by

$$f(t) = \frac{1}{C_G} \int_{-\infty}^{\infty} \int_{0}^{\infty} T(a,b)\overline{\Psi(\frac{t-b}{a})}\,\frac{da\,db}{a^2}, \tag{22}$$

and thus the wavelet transformation offers the possibilities for filtering. $C_G$ is a wavelet-dependent normalizing factor. The energy of the function $f$ is conserved since

$$\begin{aligned} \int_{-\infty}^{\infty} |f(t)|^2 &= \frac{1}{C_G} \int_{-\infty}^{\infty} \int_{0}^{\infty} |T(a,b)|^2\,\frac{da\,db}{a^2} \\ &= \frac{1}{C_G} \int_{0}^{\infty} E(a)\frac{da}{a^2}. \end{aligned} \tag{23}$$

In equation (23) the wavelet variance

$$E(a) = \int_{-\infty}^{\infty} |T(a,b)|^2 db$$

was introduced, which gives the global energy distribution of $f(t)$ along the scale $a$. Therefore $E(a)$ is equivalent to the common power spectrum calculated by means of various methods of frequency analysis, for example, the modified averaged periodogram method described by *Welch* [1967], the multitaper method used by *Mann and Park* [1994], and the maximum entropy spectral analysis reported by *Olberg and Rakoczi* [1984]. The main difference between the wavelet variance $E(a)$, sometimes termed as global wavelet power spectrum, and the common power spectrum is the inherent, scale-adapting averaging over scale (frequency) bands of the wavelet method.

In order to prove the randomness of fluctuations in the climate system, Fourier spectra of observed or modeled time series are often compared to the spectra of corresponding white or red noise processes which are obtained by fitting a first-order autoregressive (AR(1)) process to the time series. Significant differences between observed and corresponding red noise spectra are determined by means of a $\chi^2$ test applied for the calculation of confidence levels. Recently, *Torrence and Compo* [1998] used this concept for the establishing of significance levels and confidence intervals not only for the global wavelet power spectrum $E(a)$ but also for the local wavelet power spectra $E_l(a,b_0) = |T(a,b_0)|^2$. All following presentations of results of the wavelet method display local or global wavelet power spectra together with the 95% confidence levels of the corresponding AR(1) processes. The wavelet software used was provided by Torrence and Compo and is available at URL: http://paos.colorado.edu/research/wavelets/.

The identification of the scale $a$ with the commonly used frequency $\omega$ or period $T$ is not necessarily straightforward, because it depends on the specific wavelet. One way to achieve this relation [*Collineau and Brunet,* 1993; *Torrence and Compo,* 1998] is the consideration of a sine or cosine wave of a known frequency $\omega$ and the calculation of the maximum of the wavelet variance for a specific wavelet. For instance, for the complex Morlet wavelet $\Psi(t)$ =exp$(i\omega^* t)$exp$(-t^2/2)$, this procedure leads to

$$\omega = \frac{2\pi}{T} = \frac{0.5(\omega^* + \sqrt{\omega^* + 2})}{a}. \qquad (24)$$

Some attention has to be paid to the choice of the wavelet, because the results of the wavelet transformation are dependent on the characteristics of the chosen wavelet, especially on their behavior in the frequency domain [*Farge,* 1992]. In this investigation we used the Morlet wavelet with $\omega^* = 7$, which is well localized in the frequency domain and well-suited for filtering.

### 4.2. Variability of the Atmosphere-Ocean System

In the following we present results of 1000 year long simulations of the climate model using the nonstationary parameterization of synoptic-scale horizontal heat fluxes $\widehat{u'T'}$ and $\widehat{v'T'}$ and kinetic energy components $\widehat{u'^2}$ and $\widehat{v'^2}$. In order to determine the influence of the nonstationary synoptic-scale parameterization on the low-frequency variability of the large-scale atmospheric circulation pattern, we compare the results with those ones obtained by a model run performed with the fully stationary synoptic-scale parameterization according to the ratio of the annual cycle to the longer variations.

For this purpose, Figure 7 presents the first principal component of the unfiltered fivedaily averaged fields of Northern Hemispheric stream functions at 5 km for a cutout of 40 years which includes the annual cycle as the main feature as is evident in Figure 7a for both runs. To show the long-term behavior more clearly, Figure 7b presents the same cutout of 40 years of PC1 after filtering all periods smaller than 1.5 years. The introduction of the nonstationary parameterization of $\widehat{u'T'}$, $\widehat{v'T'}$, $\widehat{u'^2}$, and $\widehat{v'^2}$ increases the temporal variability on longer timescales approximately by a factor of 3. In the following the variability of the coupled atmosphere-ocean system has been analyzed from 1000 year long

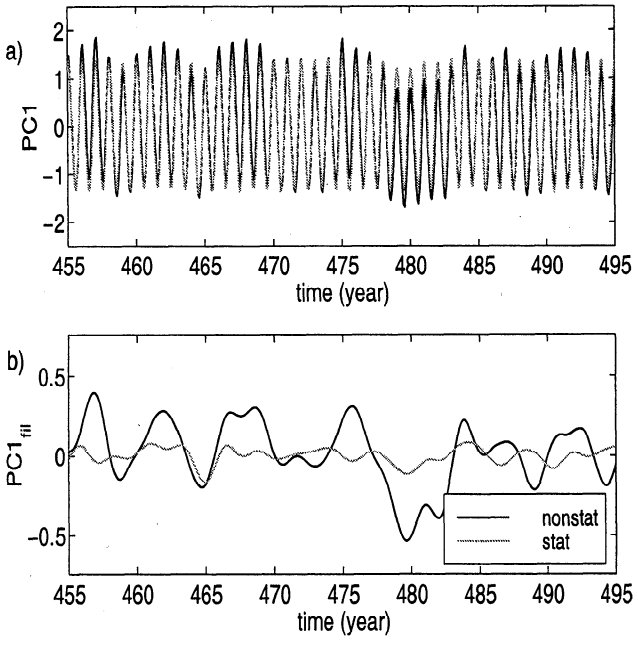


**Figure 7.** (a) First principal component of the unfiltered Northern Hemispheric stream function at 5 km for a cutout of 40 years, comparing runs with fully stationary parameterization of the second moments and with nonstationary parameterization of the synoptic scale heat and kinetic energy fluxes. (b) The same time series as those in Figure 7a but after filtering all periods smaller than 1.5 years.

model integrations performed with the nonstationary parameterization of the mentioned second moments.

The spatial structure of the dominant large-scale circulation pattern of the fully coupled atmosphere-ocean system is obtained by an EOF analysis of the annual averaged fields and displayed in Figure 8 for sea level pressure (SLP) and for stream function at 5 and 35 km height. At all heights the first mode is dominated by a wavenumber 2 with a more pronounced zonal structure at stratospheric heights. This mode is closely connected with the land-sea distribution. The first EOF explains about 63.5, 82.4, and 92.3% of total variance at sea level, 5 and 35 km, respectively. The second EOF pattern explains about 9.5, 6.9, and 3.0% of total variance at sea level, 5 and 35 km. At sea level and 5 km the EOF2 pattern contains regionally localized structures especially at midlatitudes. In the lower stratosphere, EOF2 contains mainly the long planetary waves which can propagate from tropospheric to stratospheric heights during winter. The described spatial patterns achieved from our model results can be compared with those obtained by an EOF analysis of observational data by *Wallace* [1996]. At stratospheric heights the modeled spatial structures of strong polar vortex as most dominant feature and long planetary waves as second spatial mode are confirmed by the observational analysis by Wallace. In the troposphere it seems that the leading EOFs produced by the model are more dominated by the land-sea distribution than the leading EOFs derived from observations are. The spatial pattern of EOF1 of the sea level pressure determined from our model results can be compared with the observational pattern calculated by *Wallace and Gutzler* [1981]. Their Figure 11a presents hints on a pattern with wavenumber 2, which is a strong feature in our modeled pattern. In comparison to this observational pattern, our most dominant pattern of sea level pressure is displaced southerly. This is in accordance to the overestimation of the strength of the simulated subtropical highs (see section 3). For the same reason, the strong Northern Hemispheric teleconnection patterns are not so well established as those in the observations [*Rogers,* 1981], but nevertheless, remarkable hints on these patterns can be recognized in the analyses of the model simulations. For instance, a dipole pattern similar to the NAO pattern has been found in EOF2 but with a pronounced southerly shift.

By means of the continuous wavelet transformation, we quantified the low-frequency variability connected with the most dominant spatial patterns. In Figure 9 the local and global wavelet power spectra, obtained by using the Morlet wavelet, of PC1 and PC2 for SLP and stream functions at 5 and 35 km height for the 1000 year long integration are visualized. These analyses reveal complex modes of variability for the coupled system.

The preferred timescale of variations in the first mode throughout the atmosphere has been found at the decadal scale at about 9 years, as indicated by the local and global wavelet power spectra of all PC1s. Despite the high unsteadiness, the variations on the mentioned timescale exceed the 95% confidence level of the corresponding red noise processes during the whole integration. The second mode of variability shows a less uniform temporal behavior throughout the atmosphere. Near the surface an interannual mode with a period of about 7 years and a high degree of intermittency occurs. Additionally, interdecadal variations can be estimated at periods of about 18 and 30 years. From Figure 9 it is clearly indicated that for interdecadal variations, two states exist, one is characterized by a 30 year period (model years 200-400 and 800-1000) and the other is characterized by an 18 year period (model years 0-100 and 450-750). The transition periods between these states are rather short. In the free troposphere at 5 km and in the lower stratosphere at 35 km, we find the most dominant periods of about 5-10 years with global maxima of spectral energy at 5 and 9 years. Furthermore time sections can be estimated, where variations at an interdecadal scale of about 30 years leave the 95% confidence level of the corresponding red noise processes. The time interval 450-800 years exhibits a longer breakdown of this period and coincide with the time of the presence of the 18 year period instead of the 30 year period found in the PC2 of SLP. Nevertheless, at upper heights there is no clear distinction between the two modes of interdecadal variability as described above for PC2 of SLP. Here it should be mentioned that all estimated peaks of interannual to interdecadal variability can be confirmed by traditional spectral analyses by using periodogram, maximum entropy, or multitaper methods.

To complete the above given analysis of atmospheric variables, in Figure 10 the local and global wavelet power spectra, of PC1 and PC2 of the sea surface temperature (SST), for the interactively coupled model run are presented. In contrast to the analysis of atmospheric fields, the favored timescale of the most dominant mode is about 30 years, which diminishes in the interval 450-750 years, the time of the appearance of 18 year oscillations in the time series of PC2 of SLP. Additionally, some spectral energy can be found at about 5 and 9 years. The power spectra of PC2 reveals one stable decadal mode of about 9 years.

In order to investigate the role of internal atmospheric dynamics apart from the interaction with the ocean in generating decadal and multidecadal variability, a second 1000 year long integration has been performed. In this run a forcing by a climatological annual cycle of sea surface temperature from observations has been used. Again, the synoptic-scale second moments are parameterized in the same nonstationary manner as that used before. The SST-forced integration produces essentially the same mean climate as that produced by the coupled integration.

The spatial structure (not shown) of the dominant large-scale circulation pattern is quite similar to that of the coupled run. EOF1 explains now a larger fraction

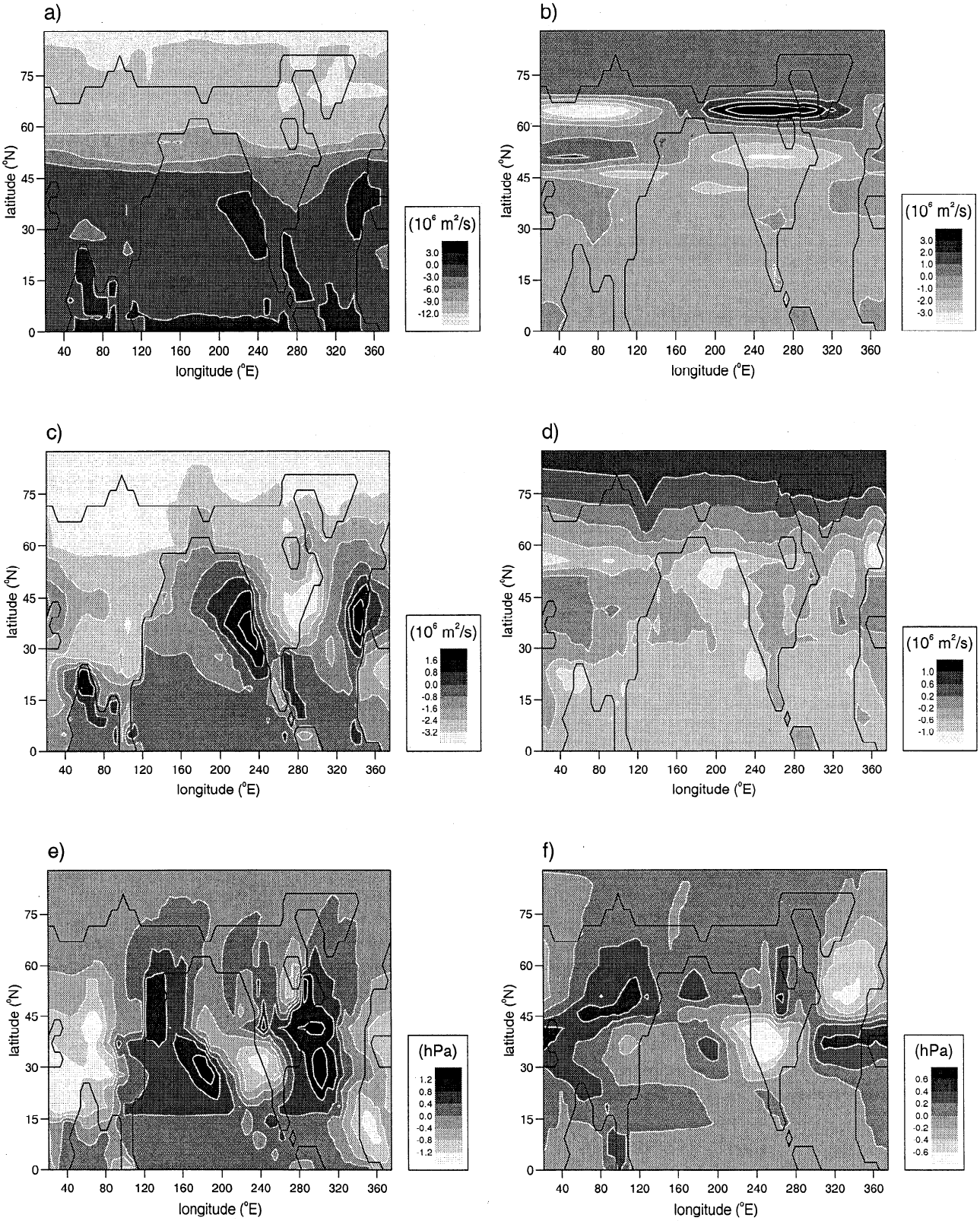


**Figure 8.** Structure of the first two empirical orthogonal functions (EOFs) of annual averaged fields of stream functions at 35 and 5 km height and of sea level pressure (SLP), obtained for the 1000 year long integration of the coupled model: (a) EOF1, 35 km; (b) EOF2, 35 km; (c) EOF1, 5 km; (d) EOF2, 5 km; (e) EOF1, SLP; (f) EOF2, SLP.

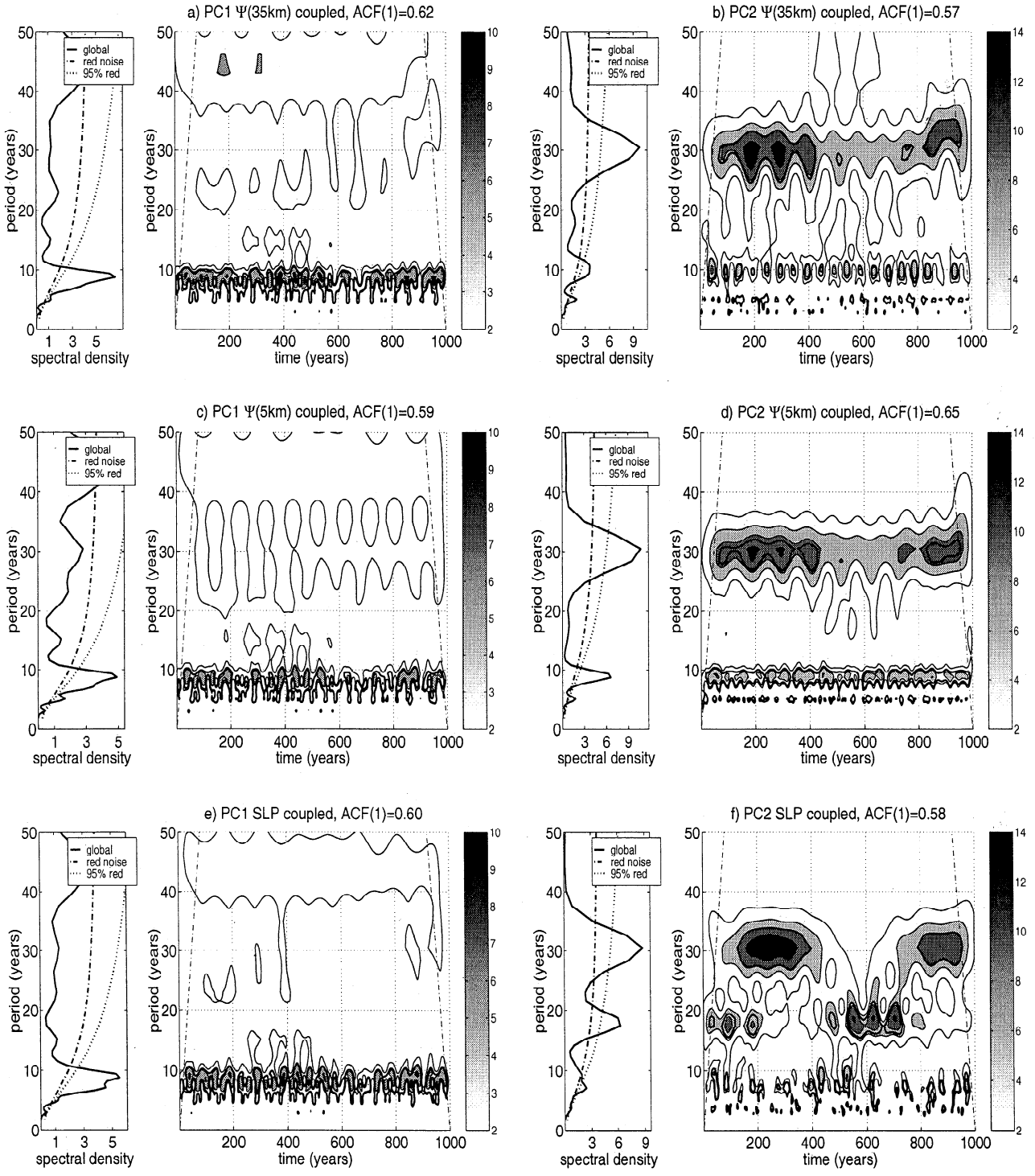


**Figure 9.** Results of wavelet transformation, performed with the Morlet wavelet, of time series of principal components obtained from the 1000 year long integration of the coupled model: (a) PC1, stream function at 35 km; (b) PC2, stream function at 35 km; (c) PC1, stream function at 5 km; (d) PC2, stream function at 5 km; (e) PC1, SLP; and (f) PC2, SLP. Left panels display the time-integrated global wavelet power spectra together with the spectrum and the 95% confidence level of a corresponding red noise process with the mentioned value of the lag-one autocorrelation function (ACF(1)). Right panels present local wavelet power spectra. At both ends, dash-dotted lines separate regions where edge effects become important. The thick contour envelopes areas of greater than 95% confidence for a corresponding red noise process with the indicated lag-one coefficient.

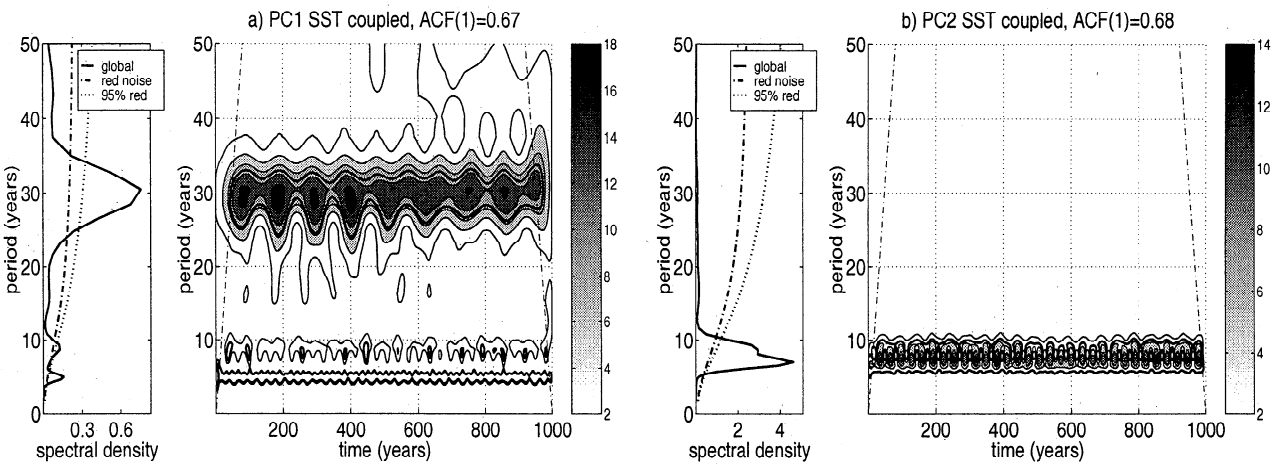


**Figure 10.** Same as in Figure 9 but for time series of (a) PC1 of sea surface temperature and (b) PC2 of sea surface temperature.

of total variance, namely, about 95.3, 97.8, and 98.1% of total variance at sea level, 5 and 35 km respectively. The EOF2 pattern explains about 1.6, 0.8, and 0.6% of total variance at sea level, 5 km and 35 km.

The results of wavelet analysis of the corresponding PCs (Figure 11) reveal a very strong and stable mode of decadal variability without any hint of intermittent behavior. This mode is detectable in the temporal variations of the first and second most dominant spatial pattern of all analyzed fields throughout the atmosphere up to 35 km height without significant shifts in the distribution of spectral energy. Preferred timescales with the maximum of the spectral energy of about 9 years can be inferred which leave the 95% confidence level of the corresponding red noise processes during the whole course of integration.

In order to evaluate the reliability of the estimated distinguished spectral peaks of the model results, we compare these issues with results of analyses of available long-term atmospheric observational data and different paleoclimate proxy data. One investigation of instrumental records of global temperature anomaly data over 100 years by *Mann and Park* [1994] identified an interdecadal mode of 15-18 years and quasi-decadal modes of 10-12 years and 7-8 years by means of a singular value decomposition. Confirmation of the existence of several decadal and interdecadal temporal modes can be obtained from examinations of different historical and paleoclimate proxy records. The frequency analysis of a 700 year long record from the Greenland Ice Sheet Project 2 (GISP2) ice core by *White et al.* [1991] presents spectral peaks of about 5, 6, and 7 to 8, and 11 to 12, 20, and 30 years. Moreover, in tree ring records some hints on interdecadal variations have been found [see, e.g., *Stuiver,* 1980].

The above presented results clearly show that climate variability on interannual to interdecadal timescales can be produced by this coupled atmosphere-ocean model with a nonstationary parameterization of synoptic-scale horizontal heat and kinetic energy fluxes. The preferred modes are supported by observational data, but the strength of these decadal to interdecadal modes is more enhanced in the model results. However, an assessment of the model results by comparison with data is limited owing to the short global instrumental records and the confined temporal and horizontal resolution of paleoclimate proxy data.

The comparison of the coupled run with the SST-forced run provided in this section leads to the conclusion that there seems to be a mode of decadal variability originated from atmospheric dynamics under the influence of seasonally varying SSTs. For the excitation of interdecadal climate variations the inclusion of oceanic processes is necessary. We are going to discuss possible causes for the identified modes of decadal and interdecadal variability of the model simulations in more detail in section 5.

### 4.3. Variability of the North Atlantic Oscillation

The analyses obtained in section 4.2 reveal that interdecadal variability is only evident in the higher-order atmospheric modes. Thus the question arises whether these interdecadal fluctuations have an influence on the climatic state of the Northern Hemisphere. Our investigations bring out hints on similarities between the temporal and spatial structure of the second mode of variability (EOF2/PC2) of the sea level pressure and of the North Atlantic Oscillation (NAO).The North Atlantic Oscillation is one of the well-known teleconnection patterns which determines to a large amount the winter climate conditions in western and middle Europe. According to *Hurrell* [1995] one definition of the NAO index is based on the normalized sea level pressure difference between Lisbon, Portugal (38.8°N, 9.1°W), and Stykk-

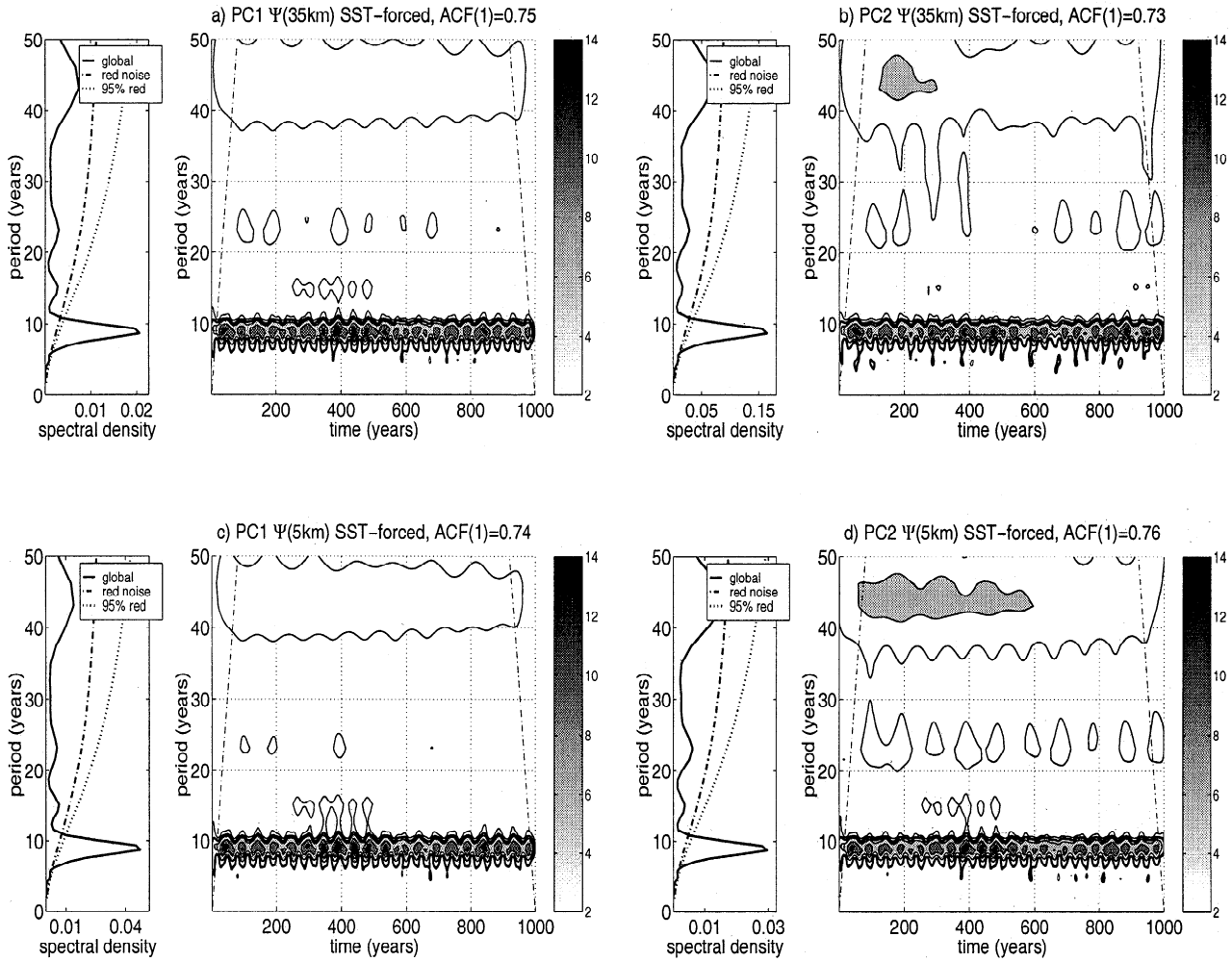


**Figure 11.** Same as in Figure 9 but for time series of principal components obtained from the 1000 year long integration of the sea surface temperature-forced model: (a) PC1, stream function at 35 km; (b) PC2, stream function at 35 km; (c) PC1, stream function at 5 km; and (d) PC2, stream function at 5 km.

isholmur, Iceland (65.1°N, 22.7°W), averaged over each winter (December-March) since 1864. High values of NAO index correspond to strengthened westerlies, with winters warmer than normal over Europe and winters colder than normal over Greenland. In order to compare observations of the NAO index with model results, the normalized sea level pressure difference between the grid points at (67°N, 24°W) and (39°N, 12°W), averaged over each winter (December-March), has been calculated for 1000 years of integration for the coupled run as well as for the SST-forced run.

The time series of the NAO index obtained for the coupled run is shown in Figure 12 together with the local and global wavelet power spectra. The latter indicate preferred timescales at 5 and 30 years with a breakdown of the 30 year period and a shift to a 18 year period in the time interval 450-750 years in accordance with the analyses of PC2 of sea level pressure. The NAO index derived from the results of the SST-forced atmosphere run is shown in Figure 13. The wavelet analysis provides favored timescales at about 3.5 and 9 years, and the disappearance of pronounced interdecadal variations is obvious.

A wavelet analysis of the time series of the observed NAO index, defined according to *Hurrell* [1995], is displayed in Figure 14 and indicates interannual (2-3 years) to decadal (about 8 years) variations in coincidence with investigations by, for example, *Hurrell and van Loon* [1997]. A similar structure of the time variations of preferred periods can be detected from arbitary cutouts of the NAO index derived from the results of the coupled run. An example for a cutout of the same length as the observed time series of the NAO index is displayed in Figure 14. The preferred timescales are more pronounced in the model than in the observations, although the overall agreement is remarkable. The more stochastic nature of the observed NAO index is supported by the low value of the lag-one autocorrelation coefficient of 0.18 in comparison with 0.42 for the modeled index. Nevertheless, under consideration of the intermittent character of decadal and interdecadal variations exhibited by the above investigations of the cou-

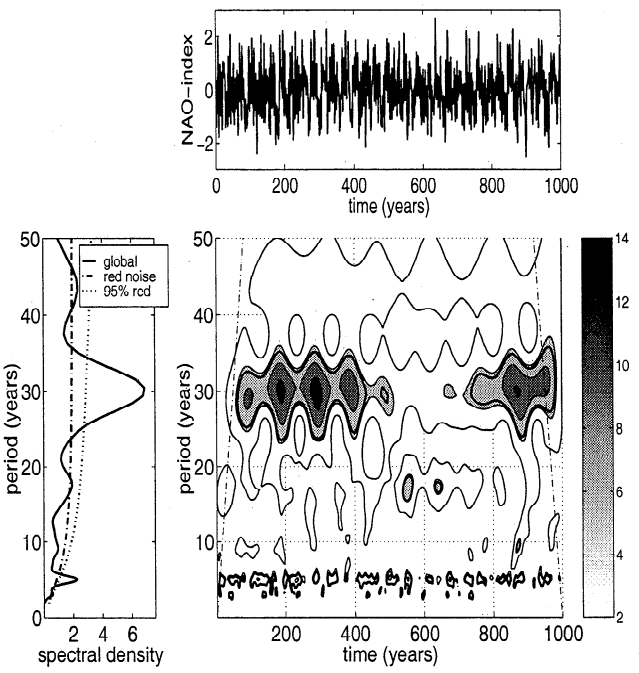


**Figure 12.** Wavelet power spectra of the time series of the North Atlantic Oscillation (NAO) index obtained from the 1000 year long integration of the coupled model, including (left) global spectra and (right) local spectra. Additionally, in the upper time series the NAO index is shown. All confidence levels correspond to a lag-one autocorrelation coefficient of 0.42. For further explanations, refer to Figure 9.

pled run, the length of the time series of observed NAO index is too short for a reliable comparison of decadal and especially interdecadal variations between model and observations.

## 5. Discussion and Conclusions

Modes of natural variability on decadal and interdecadal timescales have been investigated by means of an atmosphere-ocean climate model of moderate complexity using a nonstationary parameterization of atmospheric synoptic-scale horizontal heat and kinetic energy fluxes. The applied climate model simulates the main large-scale features of atmospheric circulation in agreement with observational data without any climate drift and presents an appropriate tool for analyzing natural climate variability. The above presented results of two long-term runs for the coupled atmosphere-ocean system and for a SST-forced atmosphere reveal a complex structure of spatial and temporal modes on decadal and interdecadal timescales. For both runs the wavelet power spectra of principal components of various atmospheric fields show significant deviations from red noise. Thus the existence of significant time periods is indicated in contrast to the assumption of purely random atmospheric fluctuations on climate timescales. Furthermore, the comparison of the results of both model runs leads to the conclusion that there exists a decadal mode generated from atmospheric dynamics itself under the influence of seasonally varying SSTs. In contrast, the interdecadal climate variations can be initiated only by the insertion of oceanic processes. These issues confirm the common understanding of natural climate variability as unforced, inherent oscillations arising primarily from atmospheric dynamics, while for interdecadal variations, subsystems of the climate system with large heat capacities or time constants, especially the ocean and its interaction with the atmosphere, must be involved.

The simplest model for the explanation of interdecadal variability is the stochastic climate model approach of *Hasselmann* [1976]. The atmospheric forcing at the synoptic scale is regarded as white noise, which is integrated by the ocean. This results in lower frequency variations of oceanic fields and produces red spectra without pronounced peaks. In view of the mentioned observed and modeled dominant interdecadal peaks, there must be additional internal mechanisms which generate these atmosphere-ocean modes. These modes have been widely treated, mostly by means of complex coupled general circulation models. *Latif* [1998] summarizes four primary mechanisms of simulated interdecadal variability: interdecadal variability originating in the tropics, interdecadal variability due to the interaction between the tropics and midlatitudes, and midlatitudinal interdecadal variability associated with wind-driven ocean gyres and with the thermohaline circulation.

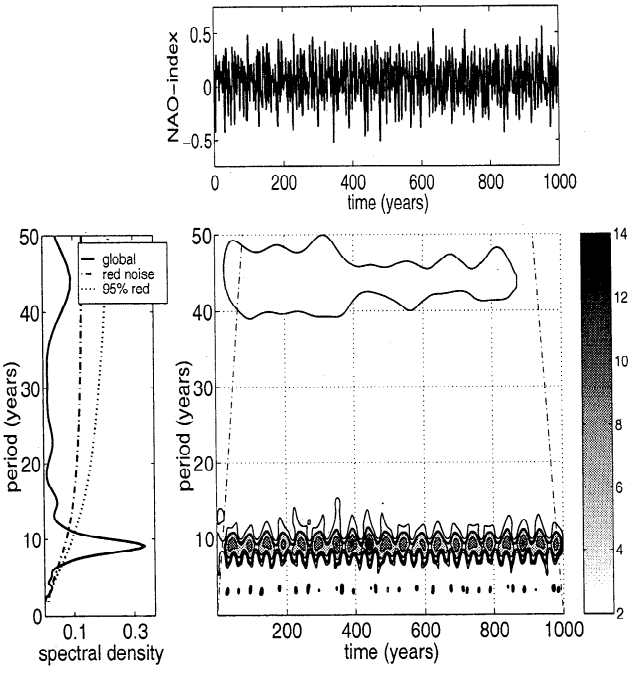


**Figure 13.** Same as in Figure 12 but for the time series of the NAO index obtained from the SST-forced run. All confidence levels correspond to a lag-one autocorrelation coefficient of 0.57.

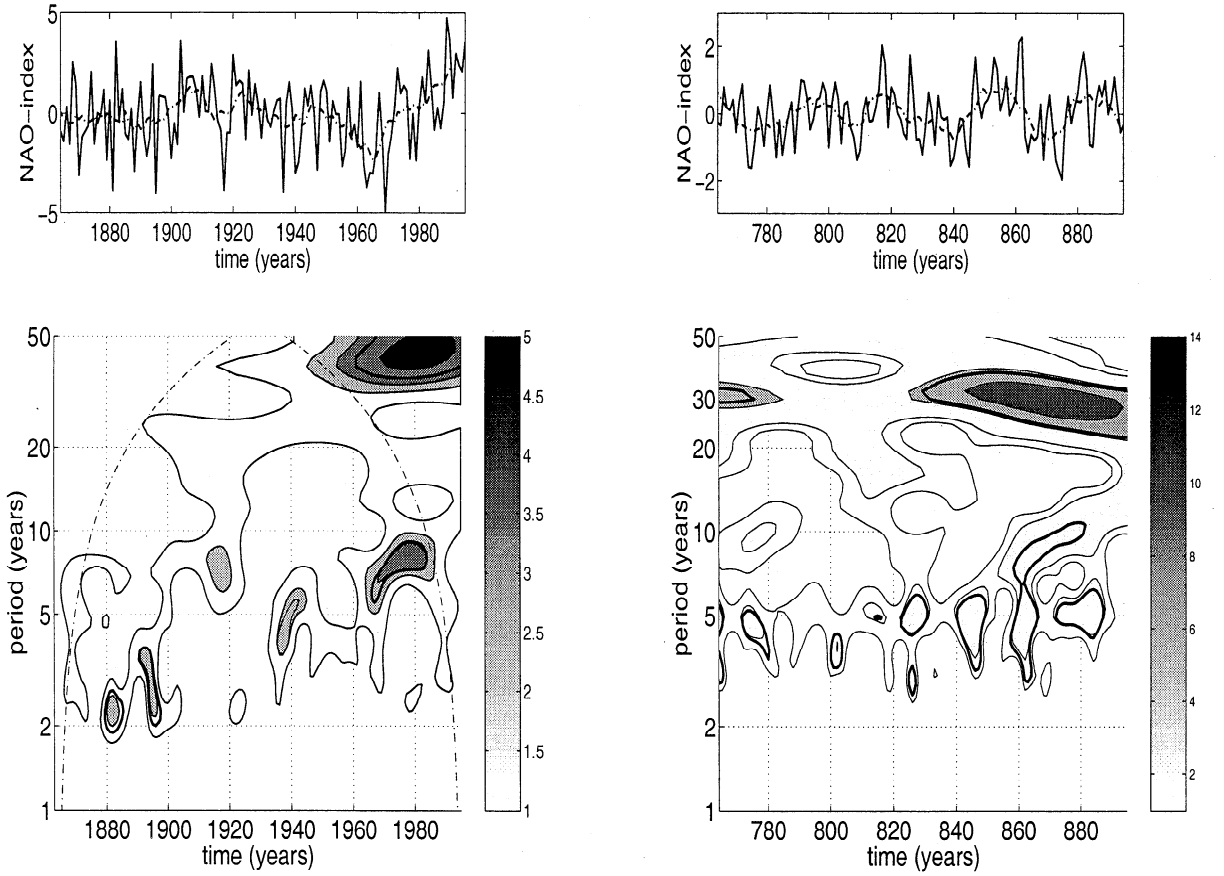


**Figure 14.** Comparison of results of (left) a wavelet transformation of the observed NAO index defined according to *Hurrell* [1995] and (right) an arbitary cutout of the NAO index, obtained from the coupled run, over 130 years. Additionally, in the upper time series the NAO indices are shown. All confidence levels correspond to a lag-one autocorrelation coefficient of 0.18 (observations) and 0.42 (coupled model run). For further explanations, refer to Figure 9.

Regarding the role of wind-driven ocean gyres, a North Pacific and a North Atlantic mode have been investigated by, for example, *Latif and Barnett* [1994], *Zorita and Frankignoul* [1997], and by *Grötzner et al.* [1998]. These studies found evidence for variations with periods between 10 and 20 years connected with a clockwise rotation of SST anomalies around the subtropical gyres with shorter periods of the North Atlantic mode [*Latif and Barnett,* 1994], which are supported by observational analysis [*Deser and Blackmon,* 1993].

The primary mechanism responsible for interdecadal variability associated with the thermohaline circulation is the driving of the strength of the overturning by density anomalies due to thermal or haline processes in the polar region. *Delworth et al.* [1993] and *Delworth* [1996] identified such a mode with a peak of about 50 years as an ocean-only mode in a multicentury run of the Geophysical Fluid Dynamics Laboratory (GFDL) model, whereas *Timmermann et al.* [1998] have found a 35 year, inherently coupled atmosphere-ocean mode by investigation of a 700 year run with the coupled complex GCM European Center/Hamburg/Large Scale Geostrophic (ECHAM3/LSG). In both studies the variations of the thermohaline circulation are mainly triggered by salinity anomalies. The mentioned coupled models employed flux corrections, and the effects of these limitations on the simulation of interdecadal variability are not yet understood. Nevertheless, much simpler models [*Chen and Ghil,* 1996; *Saravanan and McWilliams,* 1997] can generate similar interdecadal modes caused by temperature effects.

The results of the coupled atmosphere-ocean run (compare Figures 9 and 10) exhibit a strong 30 year mode, which is strongest in the fields of SST, where it is connected with the most dominant spatial pattern. In the fields of atmospheric variables this mode appears in connection with the second dominant pattern. Our results reveal that the low-frequency atmospheric variability on interdecadal scales is increased as a result of coupling the atmospheric subsystem to the oceanic subsystem in agreement with *Blade* [1997]. The interdecadal mode is generated by an atmosphere-ocean interaction, but in comparison to complex GCMs in our model, the ocean plays a more passive role, and the variability originated mainly from the atmosphere. The role of potential variations of the meridional overturning caused by temperature or thermohaline effects and of horizontal gyral circulation due to the atmosphere-ocean interaction in our model has to be clarified in future investigations.

In accordance with our results, spectral peaks at decadal and interdecadal scales have been detected by

investigations of observational data or with complex models, but our model results have revealed more pronounced peaks. By enhancing the models complexity, for example, by solving the full equation for salinity or by treating all synoptic-scale second moments in a nonstationary manner, we expect smoothed spectral peaks. However, if one considers the long-term integrations performed with different versions of ECHAM models, a significant change of the spectral behavior can be recognized. Whereas the analysis of a 1260 year long simulation of the ECHAM1/LSG model by *von Storch et al.* [1997] reveals an essentially white noise behavior on timescales longer than 1 year, Northern Hemispheric modes with significant spectral peaks between 5 and 10 years and about 35 years have been recognized from analysis of long-term runs with the improved versions of ECHAM3/LSG over 700 years [*Timmermann et al.,* 1998] and of ECHAM4/Ocean/isoPYCnal coordinates (OPYC3) model over 300 years [*Christoph et al.,* 1998].

The accentuated interdecadal variations of the most dominant mode of the SST field (see Figure 10) at about 30 years show considerable similarity with the preferred periods of the modeled NAO index (see Figure 12). This strong correlation agrees with observational studies, for example, by *Reynolds and Smith* [1994]. On the basis of monthly mean data these authors developed evidence that the SST patterns primarily reflect those of the atmospheric forcing. *Bjerknes* [1964] revealed that SST changes in the North Atlantic could be explained by the variations in the air-sea fluxes associated with changes in the winds. He argued that interdecadal SST changes are also primarily driven by the atmosphere and related to changes in the surface heat fluxes and the wind-driven circulation. Contrarily, the results obtained by *Kushnir* [1994] support the idea that SST changes are largely governed by ocean circulation changes and the atmosphere responds to these SST variations. As pointed out by *Frankignoul* [1999], the role of surface heat exchanges at very low frequencies needs to be clarified. Currently, it is not yet clear whether the ocean only passively responds to the atmospheric forcing or air-sea feedbacks increase the variability in the atmosphere and the ocean.

In comparison of the estimated features of coupled atmosphere-ocean variability, our results of the SST-forced run suggest the manifestation of atmospheric variability in a few spatial coherent structures, which are strongly linked with preferred decadal fluctuations of about 9 years, and thus we suppose that a noticeable part of the variations on this timescale can be exited from atmospheric dynamics under the influence of seasonally varying SSTs. The similarity between variations with periods of about 9 years throughout the atmosphere from sea level to upper stratospheric heights (see Figure 11) in the two most dominant modes leads to the conclusion that significant contribution to decadal climate variability can be related to atmospheric dynamical processes connected with the vertical coupling of tropospheric and stratospheric layers.

On the basis of observations of wintertime geopotential height and temperature fields, *Perlwitz and Graf* [1995] have found two natural coupled modes between the troposphere and stratosphere. One of these modes is a baroclinic one which expresses the connection between the strength of the stratospheric polar vortex and the North Atlantic tropospheric circulation. An anomalously strong vortex is coupled with strengthened tropospheric westerlies, leading to positive temperature anomalies over northern Eurasia. Because of the similarity of the tropospheric pattern with the NAO pattern, it can be proposed that this mode contributes to fluctuations of the NAO index.

Similar spatial patterns of decadal trends in the Northern Hemispheric tropo- and stratosphere have been exhibited by *Kodera and Koide* [1997] from wintertime observations over 29 years. Confirmation of these patterns is provided by GCM integrations forced by climatological SSTs without interannual variation. This provides evidence for the identification of this mode of variability connected with stronger or weaker polar night jets as an internal atmospheric mode due to the interaction between the polar vortex and planetary waves. As mentioned by Kodera and Koide, the question arises as to which processes generate the memory of this mode which is obvious only in winter. Besides the influence of changes in the radiative forcing, Kodera and Koide discussed Earth's surface processes as possible causes for producing a memory mechanism for this coupled tropospheric-stratospheric mode.

Additionally, examinations with simpler low-order atmospheric models by, for example, *Pielke and Zeng* [1994] and *Dethloff et al.* [1998] reveal considerable spectral energy on decadal and centenial timescales but without such pronounced peaks as those in our study. Experimental and modeling investigations which concentrate on the nonlinear interaction between baroclinic waves and the zonal mean flow reveal indeed a much longer timescale of $10^2$ days compared to that of the baroclinic waves. This is caused by the adjustment of zonal jets due to the growth and decay of baroclinic waves [*James et al.,* 1994; *Read et al.,* 1998]. Nevertheless, the mechanisms which link variations at this scale of $10^2$ days to those at interannual to decadal scales still have to be clarified.

The main aims of this study were to introduce a new climate model of moderate complexity to a broader community, to present results of model validation, and to exhibit the potential of the model for investigations of natural climate variability. By means of performing two 1000 year long integrations with the fully coupled atmosphere-ocean model and with the SST-forced atmospheric model, we examined especially features of decadal and interdecadal variability. On the basis of our model results and taking into account the mentioned studies by other authors, we propose that a large amount of the climate variations on the decadal timescales can be understood as the result of nonlinear atmospheric dynamical processes connected with the

vertical coupling of tropospheric and stratospheric layers. Modes of interdecadal variability have been identified as modes of the coupled atmosphere-ocean system which potentially can be generated by variations of horizontal gyral flows or by changes of meridional oceanic overturning. The identification of specific mechanisms that cause decadal and interdecadal variability is now our task for future studies in which we want to concentrate on the influence of nonlinear coupling between tropospheric, stratospheric, and mesospheric layers on the decadal and interdecadal climate variability.

Furthermore, the agreement between the preferred modes inferred from the wavelet analyses of the principal components of Northern Hemispheric stream functions and of the NAO index supports the view that the model atmosphere fluctuates between a preferred high-index state with strong zonal flow and weak planetary waves and a low-index state with pronounced planetary waves and weak zonal flow. This is confirmed by results of integrations of simple atmospheric low-order models. These models showed the existence of multiple large-scale equilibria states [e.g., *Egger,* 1978; *Charney and DeVore,* 1979]. Already in the early work of *Rossby et al.* [1939] the idea of generating climate fluctuations by changes in the frequency of the occurrence of high-index and low-index states was introduced. Today such a view is confirmed in the framework of nonlinear dynamics in the sense that climate fluctuations on longer timescales are caused by changes of the probability density functions of nonlinear weather regimes [*Palmer,* 1998; *Corti et al.,* 1999]. As mentioned above, some specific mechanisms leading to interdecal variations of the climate system have been already detected, but especially the contribution of atmospheric nonlinear processes to changes of regime frequency has not been understood. The latter has to be determined by future studies in order to assess the influence of anthropogenic changes on the climate system.

**Acknowledgments.** The authors appreciate the very useful comments of the anonymous reviewers which helped to improve the manuscript. The work was partly sponsored by the strategy fund project 'Natural climate variations from 10,000 years to the present day' of the Helmholtz Association of German Research Centres (HGF). Additional support was provided by the Russian Foundation for Basic Research. This study is AWI contribution 1469.

## References

Andrews, D. G., J. R. Holton, and C. B. Leovy, *Middle Atmosphere Dynamics,* 489 pp., Academic, San Diego, Calif., 1987.

Baliunas, S., P. Frick, D. Sokoloff, and W. Soon, Time scales and trends in the Central England Temperature data (1659-1990): A wavelet analysis, *Geophys. Res. Lett., 24,* 1351-1354, 1997.

Bjerknes, J., Atlantic air-sea interaction, *Adv. Geophys., 10,* 1-82, 1964.

Blade, I., The influence of mid-latitude coupling on the low-frequency variability of a GCM, *J. Clim., 10,* 2087-2106, 1997.

Boville, B. A., and P. R. Gent, The NCAR Climate System Model, version one, *J. Clim., 11,* 1115-1130, 1998.

Bryan, K., Climate and ocean circulation, III, The ocean model, *Mon. Weather Rev., 97,* 806-827, 1969.

Charney, J., and J. G. DeVore, Multiple flow equilibria in the atmosphere and blocking, *J. Atmos. Sci., 36,* 1205-1226, 1979.

Charney, J., and P. Drazin, Propagation of planetary-scale disturbances from the lower into the upper atmosphere, *J. Geophys. Res., 66,* 83-109, 1961.

Chen, F., and M. Ghil, Interdecadal variability in a hybrid coupled ocean-atmosphere model, *J. Phys. Oceanogr., 26,* 1561-1578, 1996.

Christoph, M., U. Ulbrich, J. M. Oberhuber, and E. Roeckner, The role of ocean dynamics for low-frequency fluctuations of the NAO in a coupled ocean-atmosphere GCM, MPI Rep., *285,* 27 pp., Max Planck Institute, Hamburg, Germany, 1998.

Collineau, S., and Y. Brunet, Detection of turbulent coherent motions in a forest canopy, I, Wavelet analysis, *Boundary Layer Meteorol., 65,* 357-379, 1993.

Corti, S., F. Molteni, and T. N. Palmer, Signature of recent climate change in frequencies of natural atmospheric circulation regimes, *Nature, 398,* 799-802, 1999.

Deardorff, J. W., Dependence of air-sea transfer coefficients on bulk stability, *J. Geophys. Res., 73,* 2549-2557, 1968.

Delworth, T., North Atlantic interannual variability in a coupled ocean-atmosphere model, *J. Clim., 9,* 2356-2375, 1996.

Delworth, T., S. Manabe, and R. J. Stouffer, Interdecadal variations of the thermohaline circulation in a coupled ocean-atmosphere model, *J. Clim., 6,* 1993-2011, 1993.

Deser, C., and M. L. Blackmon, Surface climate variations over the North Atlantic Ocean during winter: 1900-1989, *J. Clim., 6,* 1743-1753, 1993.

Dethloff, K., A. Weisheimer, A. Rinke, D. Handorf, M. V. Kurgansky, W. Jansen, P. Maaß, and P. Hupfer, Climate variability in a nonlinear atmosphere-like dynamical system, *J. Geophys. Res., 103,* 25,957-25,966, 1998.

Dickinson, R. E., A. Henderson-Sellers, P. J. Kennedy, and M. F. Wilson, Biosphere Atmosphere Transfer Scheme (BATS) for the NCAR Community Climate Model, *NCAR Tech. Note, NCAR/TN-75+STR,* 69 pp., 1986.

Egger, J., Dynamics of blocking highs, *J. Atmos. Sci., 35,* 1788-1801, 1978.

Eliseev, A. V., I. I. Mokhov, and V. K. Petukhov, Modelling the quasi-biennial oscillations of atmospheric temperature and the tendencies of its evolution under climatic changes, *Izv. Acad. Sci. USSR Atmos. Oceanic Phys., Engl. Transl., 33,* 679-687, 1997.

Farge, M., Wavelet transforms and their application to turbulence, *Annu. Rev. Fluid Mech., 24,* 395-457, 1992.

Frankignoul, C., Sea surface temperature variability in the North Atlantic: Monthly to decadal time scales, in *Beyond El Nino,* edited by A. Navarra, pp. 25-48, Springer-Verlag, New York, 1999.

Gates, W. L., et al., An overview of the results of the atmospheric model intercomparison project (AMIP I), *Bull. Am. Meteorol. Soc., 80,* 29-55, 1999.

Grötzner, A., M. Latif, and T. P. Barnett, A decadal climate cycle in the North Atlantic Ocean as simulated by the ECHO coupled GCM, *J. Clim., 11,* 831-847, 1998.

Gulev, S. K., I. I. Zveryaev, and I. I. Mokhov, Tropospheric lapse rate in dependence on surface air temperature, *Izv. Acad. Sci. USSR Atmos. Oceanic Phys., Engl. Transl., 27,* 419-430, 1991.

Hansen, J., G. Russel, D. Rind, P. Stone, A. Lacis, S. Lebedeff, R. Ruedy, and L. Travis, Efficient three-dimensional global models for climate studies: Models I and II, *Mon. Weather Rev., 111,* 609-662, 1983.

Hansen, J., et al., Forcings and chaos in interannual to decadal climate change, *J. Geophys. Res., 102,* 25,679-25,720, 1997.

Hasselmann, K., Stochastic climate models, 1, Theory, *Tellus, Ser. A, 28,* 473-485, 1976.

Hunt, B. G., and H. L. Davies, Mechanism of multi-decadal climatic variability in a global climatic model, *Int. J. Climatol., 17,* 565-580, 1997.

Hurrell, J. W., Decadal trends in the North Atlantic Oscillation: Regional temperatures and precipitation, *Science, 269,* 676-679, 1995.

Hurrell, J. W., and H. van Loon, Decadal variations associated with the North Atlantic Oscillation, *Clim. Change, 36,* 301-326, 1997.

James, I. N., and P. M. James, Ultra-low-frequency variability in a simple atmospheric circulation model, *Nature, 342,* 53-55, 1989.

James, I. N., and P. M. James, Spatial structure of ultra-low-frequency variability of the flow in a simple atmospheric circulation model, *Q. J. R. Meteorol. Soc., 118,* 1211-1233, 1992.

James, P. M., K. Fraedrich, and I. N. James, Wave-zonal-flow interaction and ultra-low-frequency variability in a simplified global circulation model, *Q. J. R. Meteorol. Soc., 120,* 1045-1067, 1994.

Khrgian, A. K. *Atmospheric Physics* (in Russian), 566 pp., Gidriometeoizdat, Leningrad, Russia, 1978.

Kodera, K., and H. Koide, Spatial and seasonal characteristics of recent decadal trends in the northern hemispheric troposphere and stratosphere, *J. Geophys. Res., 102,* 19,433-19,447, 1997.

Kraichnan, R. H., The closure problem of turbulence theory, in *Proceedings of Symposia in Applied Mathematics,* vol. XIII, *Hydrodynamic Instability,* pp. 199-225, Am. Math. Soc., Providence, R. I., 1962.

Kumar, P., and E. Foufoula-Georgiou, Wavelet analysis for geophysical applications, *Rev. Geophys., 35,* 385-412, 1997.

Kurgansky, M. V., K. Dethloff, I. A. Pisnichenko, H. Gernandt, F.-M. Chmielewski, and W. Jansen, Long-term climate variability in a simple, nonlinear atmospheric model, *J. Geophys. Res., 101,* 4299-4314, 1996.

Kushnir, Y., Interdecadal variations in North Atlantic sea surface temperature and associated atmospheric conditions, *J. Clim., 7,* 142-157, 1994.

Latif, M., Dynamics of interdecadal variability in coupled ocean-atmosphere models, *J. Clim., 11,* 602-624, 1998.

Latif, M., and T. P. Barnett, Causes of decadal climate variability over the North Pacific and North America, *Science, 266,* 634-637, 1994.

Lau, K.-M., and H. Weng, Climate signal detection using wavelet transform: How to make a time series sing, *Bull. Am. Meteorol. Soc., 76,* 2391-2402, 1995.

Manabe, S., and R. J. Stouffer, Low-frequency variability of surface air temperature in a 1000-year integration of a coupled atmosphere-ocean-land surface model, *J. Clim., 9,* 376-393, 1996.

Mann, M., and E. J. Park, Global-scale modes of surface temperature variability on interannual to century timescales, *J. Geophys. Res., 99,* 25,819-25,833, 1994.

Mitchell, J. M., An overview of climatic variability and its causal mechanisms, *Quat. Res., 6,* 481-493, 1976.

Mokhov, I. I., V. A. Bezverkhny, and A. V. Eliseev, Quasi-biennial oscillations of the atmospheric temperature regime: Tendencies of change, *Izv. Acad. Sci. USSR Atmos. Oceanic Phys., Engl. Transl., 33,* 579-587, 1997.

Mokhov, I.I., V.K. Petukhov, and V.A. Semenov, Multiple intraseasonal temperature regimes and their evolution in the IAP RAS climate model. *Izv. Acad. Sci. USSR Atmos. Oceanic Phys., Engl. Transl., 34,* 145-152, 1998.

Nakamura, M., P. H. Stone, and J. Marotzke, Destabilization of the thermohaline circulation by atmospheric eddy transports, *J. Clim., 7,* 1870-1882, 1994.

Olberg, M., and F. Rakoczi *Informationstheorie in Meteorologie und Geophysik,* 181 pp., Akademie, Berlin, 1984.

Palmer, T. N., Nonlinear dynamics and climate change: Rossby's legacy, *Bull. Am. Meteorol. Soc., 79,* 1411-1423, 1998.

Perlwitz, J., and H.-F. Graf, The statistical connection between tropospheric and stratospheric circulation of the northern hemisphere in winter, *J. Clim., 8,* 2281-2295, 1995.

Petoukhov, V. K., Zonal climatic model of heat and moisture exchange in the atmosphere over the underlying layer (in Russian), in *Physics of the Atmosphere and the Problem of Climate,* edited by G. S. Golitsyn and A. M. Yaglom, pp. 8-41, Nauka, Moscow, 1980.

Petoukhov, V. K., Dynamical-statistical modelling of large-scale climatic processes (in Russian), D.Sc. thesis, 431 pp., Leningrad Hydrometorol. Inst., St. Petersburg, Russia, 1991.

Petoukhov, V. K., and A. V. Ganopolski, A set of climate models for integrated modelling of climate change impacts, *IIASA Rep. WP-94-39,* 96 pp., Internat. Institute Appl. Systems Anal., Laxenburg, Austria, 1994.

Petoukhov, V. K., I. I. Mokhov, A. V. Eliseev, and V. A. Semenov, The IAP RAS Global Climate Model, *Tech. Rep.,* 110 pp., Moscow State Univ., Moscow, Russia, 1998.

Pielke, R. A., and H. Zeng, Long-term variability of climate, *J. Atmos. Sci., 51,* 155-159, 1994.

Preisendorfer, R. W., *Principal Component Analysis in Meteorology and Oceanography,* 425 pp., Elsevier, New York, 1988.

Read, P. L., M. Collins, W.-G. Früh, S. R. Lewis, and A. F. Lovegrove, Wave interactions and baroclinic chaos: A paradigm for long timescale variability in planetary atmospheres, *Chaos Solitons Fractals, 9,* 231-249, 1998.

Reynolds, R. W., and T. M. Smith, Improved global sea surface temperature analyses using optimum interpolation, *J. Clim., 9,* 2958-2972, 1994.

Rogers, J. C., Spatial variability of seasonal sea-level pressure and 500-mb height anomalies, *Mon. Weather Rev., 109,* 2093-2106, 1981.

Rossby, C.-G., et al., Relation between variations in the intensity of the zonal circulation of the atmosphere and the displacements of the semi-permanent centers of action, *Tellus, 2,* 275-301, 1939.

Saltzman, B., and A. D. Vernekar, An equilibrium solution for the axially symmetric component of the Earth's macroclimate, *J. Geophys. Res., 76,* 1498-1524, 1971.

Saravanan, R., and J. C. McWilliams, Stochasticity and spatial resonance in interdecadal climate fluctuations, *J. Clim., 10,* 2299-2320, 1997.

Schneider, E., and R. S. Lindzen, Axially symmetric steady state models of the basic state of instability and climate studies, I, Linearized calculations, *J. Atmos. Sci., 34,* 253-279, 1977.

Shea, D. J., S. J. Worley, I. A. Stern and T. J. Hoar, An introduction to atmospheric and oceanographic data, *NCAR Tech. Note, NCAR/TN-404+IA,* 132 pp., 1994.

Slonovsky, V. C., L. A. Mysak, and J. Derome, Linking Arctic sea ice and atmospheric circulation anomalies on interannual and decadal time scales, *Atmos. Ocean, 35,* 333-366, 1997.

Stepanov, V.N., *World Ocean* (in Russian), 254 pp., Znanie, Moscow, 1974.

Stuiver, M., Solar variability and climatic change during the current millenium, *Nature, 286,* 868-871, 1980.

Tett, S. F. B., T. C. Johns, and J. F. B. Mitchell, Global and regional variability in a coupled AOGCM, *Clim. Dyn., 13,* 303-323, 1997.

Timmermann, A., M. Latif, R. Voss, and A. Grötzner, Northern Hemispheric interdecadal variability: A coupled air-sea mode, *J. Clim., 11,* 1906-1931, 1998.

Torrence, C., and G. P. Compo, A practical guide to wavelet analysis, *Bull. Am. Meteorol. Soc., 79,* 61-78, 1998.

van der Hoven, I., Power spectrum of horizontal wind speed in the frequency range from 0.0007 to 900 cycles per hour, *J. Meteorol., 14,* 160-164, 1957.

van Mieghem, J., *Atmospheric Energetics,* 306 pp., Clarendon, Oxford, England, 1973.

Vinnichenko, N. K., The kinetic energy spectrum in the free atmosphere: 1 second to 5 years, *Tellus, 22,* 158-166, 1970.

von Storch, J., V. Kharin, U. Cubasch, G.C. Hegerl, D. Schriever, H. von Storch, and E. Zorita, A description of a 1260 year control integration with the coupled ECHAM1/ LSG general circulation model, *J. Clim., 10,* 1525-1543, 1997.

Wallace, J. M., Observed climatic variability: Spatial structure, in *Decadal Climate Variability: Dynamics and Predictability,* edited by D. L. T. Anderson and J. Willebrand, *NATO ASI Ser., Ser. I, 44,* 31-81, 1996.

Wallace, J. M., and D. S. Gutzler, Teleconnections in the geopotential height field during the northern hemisphere winter, *Mon. Weather Rev., 109,* 784-812, 1981.

Welch, P.D., The use of Fast Fourier Transform for the estimation of power spectra: A method based on time averaging over short modified periodograms, *IEEE Trans. Audio Electroacoust., AU-15,* 70-73, 1967.

Werner, P., and H. von Storch, Interannual variability of central European mean temperature in January/February and its relation to the large-scale circulation, *Clim. Res., 3,* 195-207, 1993.

White, W. C., D. Gorodetzky, E. R. Cook, and L. K. Barlow, Frequency analysis of an annually resolved, 700 year paleoclimate record from the GISP2 ice core, in *Climatic Variations and Forcing Mechanisms of the Last 2000 Years,* edited by P. D. Jones, R. S. Bradley, and J. Jouzel, *NATO ASI Ser., Ser. I, 41,* 193-212, 1991.

Zorita, E., and C. Frankignoul, Modes of North Atlantic decadal variability in the ECHAM1/ LSG coupled ocean-atmosphere general circulation model, *J. Clim., 10,* 183-200, 1997.

K. Dethloff, D. Handorf, and A. Weisheimer, Alfred Wegener Institute for Polar and Marine Research, Telegrafenberg A 43, D-14473 Potsdam, Germany. (dethloff@awi-potsdam.de; dhandorf@awi-potsdam.de; weisheim@awi-potsdam.de)

A. V. Eliseev, I. I. Mokhov, and V. K. Petoukhov, Obukhov Institute of Atmospheric Physics, Russian Academy of Sciences, Pyzhevsky 3, 109017 Moscow, Russia. (lesha@omega.ifaran.ru; mokhov@omega.ifaran.ru)

(Received December 21, 1998; revised July 20, 1999; accepted July 28, 1999.)